NAVAL POSTGRADUATE SCHOOL

MONTEREY, CALIFORNIA

THESIS

CROSS BODY THRUSTER CONTROL AND MODELING OF A BODY OF REVOLUTION AUTONOMOUS UNDERWATER VEHICLE

by

Sean Michael Doherty

March 2011

Thesis Advisor:	Douglas Horner
Second Reader:	Oleg Yakimenko

Approved for public release; distribution is unlimited

THIS PAGE INTENTIONALLY LEFT BLANK

REPORT DOCUMENTATION PAGE			*Form Approved OMB No. 0704-0188*
Public reporting burden for this collection of information is estimated to average 1 hour per response, including the time for reviewing instruction, searching existing data sources, gathering and maintaining the data needed, and completing and reviewing the collection of information. Send comments regarding this burden estimate or any other aspect of this collection of information, including suggestions for reducing this burden, to Washington headquarters Services, Directorate for Information Operations and Reports, 1215 Jefferson Davis Highway, Suite 1204, Arlington, VA 22202-4302, and to the Office of Management and Budget, Paperwork Reduction Project (0704-0188) Washington DC 20503.			
1. AGENCY USE ONLY ***(Leave blank)***	**2. REPORT DATE** March 2011	**3. REPORT TYPE AND DATES COVERED** Master's Thesis	
4. TITLE AND SUBTITLE Cross Body Thruster Control for a Body of Revolution Autonomous Underwater Vehicle		**5. FUNDING NUMBERS**	
6. AUTHOR(S) Sean Michael Doherty			
7. PERFORMING ORGANIZATION NAME(S) AND ADDRESS(ES) Naval Postgraduate School Monterey, CA 93943-5000		**8. PERFORMING ORGANIZATION REPORT NUMBER**	
9. SPONSORING /MONITORING AGENCY NAME(S) AND ADDRESS(ES) N/A		**10. SPONSORING/MONITORING AGENCY REPORT NUMBER**	
11. SUPPLEMENTARY NOTES The views expressed in this thesis are those of the author and do not reflect the official policy or position of the Department of Defense or the U.S. Government. IRB Protocol number n/a			
12a. DISTRIBUTION / AVAILABILITY STATEMENT Approved for public release; distribution is unlimited		**12b. DISTRIBUTION CODE**	

13. ABSTRACT

Cross body thrusters permit a body of revolution Autonomous Underwater Vehicle to retain the energy efficiency of forward travel while increasing the ability to maneuver in confined areas such as harbors and piers. This maneuverability also permits more deliberate underwater surveys using a fixed, mounted forward and downward looking sonar. This work develops the necessary hydrodynamic coefficients, using methods applied to earlier vehicles, to develop a valid computer simulation model. Additionally, this work develops a polynomial regression translating thruster input in RPM to an applied force output, which is incorporated into the vehicle model. This model is then employed to examine the response and control, specifically at low speed, of a body-of-revolution Autonomous Underwater Vehicle equipped with off-axis cross-body thrusters. These results are then utilized to develop a series of PID controllers for use onboard the REMUS Autonomous Underwater Vehicle.

14. SUBJECT TERMS Autonomous, Underwater, Vehicle, AUV, Thruster, Control, REMUS, Modeling, Body of Revolution			**15. NUMBER OF PAGES** 115
			16. PRICE CODE
17. SECURITY CLASSIFICATION OF REPORT Unclassified	**18. SECURITY CLASSIFICATION OF THIS PAGE** Unclassified	**19. SECURITY CLASSIFICATION OF ABSTRACT** Unclassified	**20. LIMITATION OF ABSTRACT** UU

NSN 7540-01-280-5500

Standard Form 298 (Rev. 2-89)
Prescribed by ANSI Std. 239-18

THIS PAGE INTENTIONALLY LEFT BLANK

Approved for public release; distribution is unlimited

CROSS BODY THRUSTER CONTROL AND MODELING OF A BODY OF REVOLUTION AUTONOMOUS UNDERWATER VEHICLE

Sean Michael Doherty
Lieutenant, United States Navy
B.S., United States Naval Academy, 2005

Submitted in partial fulfillment of the
requirements for the degree of

MASTER OF SCIENCE IN MECHANICAL ENGINEERING

from the

NAVAL POSTGRADUATE SCHOOL
March 2011

Author: Sean Michael Doherty

Approved by: Douglas P. Horner
Thesis Advisor

Oleg Yakimenko
Second Reader

Knox T. Millsaps
Chair, Department of Mechanical and Aerospace Engineering

THIS PAGE INTENTIONALLY LEFT BLANK

ABSTRACT

Cross body thrusters permit a body of revolution Autonomous Underwater Vehicle to retain the energy efficiency of forward travel while increasing the ability to maneuver in confined areas such as harbors and piers. This maneuverability also permits more deliberate underwater surveys using a fixed, mounted forward and downward looking sonar. This work develops the necessary hydrodynamic coefficients, using methods applied to earlier vehicles, to develop a valid computer simulation model. Additionally, this work develops a polynomial regression translating thruster input in RPM to an applied force output, which is incorporated into the vehicle model. This model is then employed to examine the response and control, specifically at low speed, of a body-of-revolution Autonomous Underwater Vehicle equipped with off-axis cross-body thrusters. These results are then utilized to develop a series of PID controllers for use onboard the REMUS Autonomous Underwater Vehicle.

THIS PAGE INTENTIONALLY LEFT BLANK

TABLE OF CONTENTS

THIS PAGE INTENTIONALLY LEFT BLANK

LIST OF FIGURES

THIS PAGE INTENTIONALLY LEFT BLANK

LIST OF TABLES

THIS PAGE INTENTIONALLY LEFT BLANK

LIST OF ACRONYMS AND ABBREVIATIONS

AUV – Autonomous Underwater Vehicle

CB – Center of Buoyancy

CG – Center of Gravity

DCC – Disturbance Compensation Controller

DOF – Degree of Freedom

EKF – Extended Kalman Filter

FLS – Forward Looking Sonar

FLT – Forward Lateral Thruster

FVT – Forward Vertical Thruster

MCM – Mine Countermeasure Operations

MRAC – Model Reference Adaptive Control

NED – North-East-Down Reference Frame

PD – Proportional Derivative Controller

PI – Proportional Integral Controller

PID – Proportional Integral Derivative Controller

REMUS – Remote Environmental Measuring UnitS

ROV - Remotely Operated Vehicle

SLAM – Simultaneous Localization And Mapping

SLT – Stern Lateral Thruster

SMC – Sliding Mode Controller

SVT – Stern Vertical Thruster

THIS PAGE INTENTIONALLY LEFT BLANK

ACKNOWLEDGMENTS

Foremost, this work would not have been possible without the advice, guidance and assistance from my thesis advisors, Professors Doug Horner and Oleg Yakimenko. To them, I owe tremendous thanks for allowing me this opportunity and providing the freedom to conduct the research on my own terms.

To all the members of the Center for Autonomous Vehicle Research at NPS, I owe a debt of gratitude for allowing me to constantly invade their workspace and pester them with ceaseless questions.

Finally, to my wife, whom I can never thank enough, I apologize for the long hours of incessant ‘Goldblum-ing.’

THIS PAGE INTENTIONALLY LEFT BLANK

I. INTRODUCTION

A. AUTONOMOUS UNDERWATER VEHICLES — A HISTORICAL PERSPECTIVE

The concept of an underwater vehicle is not new; Leonardo da Vinci envisioned submersible troop transports, assault craft, and diving rigs in the early sixteenth century.

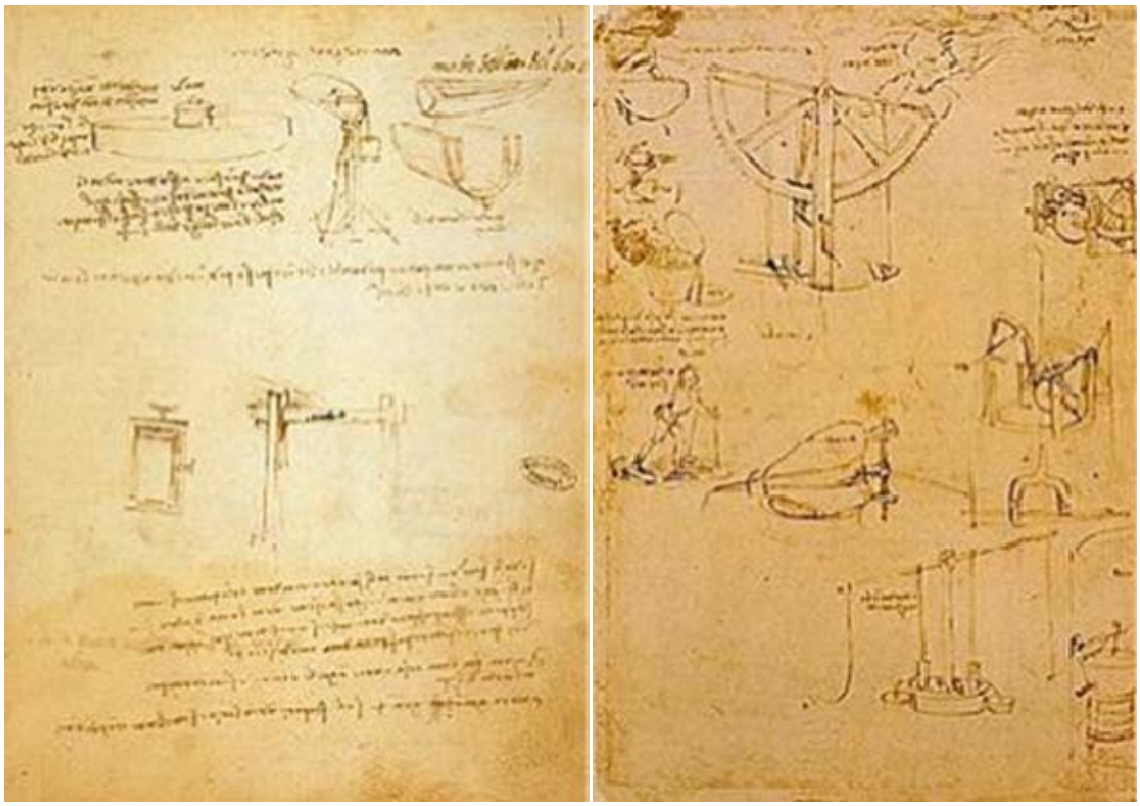

Figure 1. Da Vinci's sketch of a manned submersible, upper-left, [1] and diving rig, right, [2] circa 1500.

Ultimately, the idea remained on paper only, as full realization extrapolated from practical test results was deemed too dangerous by Da Vinci [3]. Nearly three centuries later, the Bushnell brothers built the first American submarine, the Turtle, in 1775. The tiny, single-seat, egg-shaped craft attempted the first recorded, and ultimately unsuccessful, submarine attack in New York Harbor in 1776, against the HMS Eagle [4]. Military applications of underwater vehicles have steadily marched forward since.

Parallel to the development of manned undersea vehicles, came the creation of undersea weapons systems, principally the advent of the torpedo—the first true autonomous underwater vehicle [5].

The Naval Warfare strategy of the United States constantly evolves and adapts to a varied array of threats in the dynamic and globalized modern world. Technological advances in recent years have seen a tremendous increase in the use of autonomous or remotely operated vehicles. These vehicles provide combat commanders a real-time intelligence and communications capability previously unheard of on the battlefield. As the focus of naval operations has shifted from the open ocean ("blue water") to the littoral ("green water") zones, the need for a capable and advanced autonomous underwater vehicle (AUV) has steadily increased.

The AUV provides commanders a vital near-shore intelligence and communications asset. For example, a mission profile may require the ingress of special operations personnel onto a beach via submarine. The AUV would enable the mission commander to receive real-time data from the proposed line of advance, without endangering any personnel. Furthermore, that same AUV could be used as a communications relay from the special operations team back to the submarine.

In the civilian sector, AUVs and their tethered brethren, remotely operated vehicles (ROV), have been used extensively in salvage operations. Woods Hole Oceanographic Institution's ROV *Argo*, for instance, was a primary tool used in discovering the wreck of the *Titanic* [6]. The tethered submersible enabled 24-hour reconnaissance of the wreck site at depths of almost 2.5 miles while the research teams remained above the surface.

More recently, the Deepwater Horizon (British Petroleum) Oil Spill in the Gulf of Mexico, employed teams of ROVs in several efforts to stem the flow from the leaking pipe. These ROVs featured fully maneuverable actuator arms and were operating in depths of nearly 1 mile [7]. These depths are well beyond the limit of human physiology, as the depth limit for a surface supplied diver is 285 feet [8].

The AUV provides the next step in the advancement of underwater robotic technology. While the removal of the human element entirely from the vehicle control interface requires complex and detailed control algorithms, the benefits far outstrip the risks involved in unmanned undersea vehicle operations:

- Un-tethered vehicles enable reconnaissance through a larger range, providing a cost-effective method of narrowing a search area for future study
- The AUV is programmed with its own logic algorithms, enabling instantaneous on-board decision making based on current sensory information
- No external interface is required – that is, all power and maneuvering controls are internal to the vehicle
- The AUV can operate in depths and temperatures human divers cannot
- Generally, AUVs are cheaper than ROVs, as they do not require a tethered support platform with the requisite human interface for mission accomplishment

B. MOTIVATION

Of specific interest to this thesis, is the use of AUVs in mine countermeasure and clearance operations. AUVs provide a safe and cost-effective means of determining the size of a minefield and the specific locations of individual mines. Future AUVs may even incorporate onboard mine countermeasures to defeat or disable encountered mines without endangering Naval personnel; providing a similar capability as the remotely operated ordinance disposal robots provide to U.S. military and law enforcement departments. To facilitate this, precise control in all six degrees-of-freedom during low-speed operations is required. This work will study the control and guidance of a body-of-revolution ("torpedo-like") AUV fitted with cross-body thrusters. These thrusters provide greater control and maneuverability at slow speeds than a standard single propulsor counterpart. Control surfaces require a minimum speed of advance in order to

provide effective lift to the body; consequently, this speed may be faster than the optimal resolution capability of the onboard sensors, specifically the sonar. Cross-body thrusters provide near-instantaneous control in all six degrees of freedom, enabling full 360-degree analysis of an "interesting" object as well as more "cost-effective" path planning, waypoint navigation and hovering methods.

C. LITERATURE REVIEW

Cross-body thruster control of an AUV is not a novel idea. Several AUVs, past and present, use cross-body thrusters including, among others: NPS Phoenix (c. 1996–1999), NPS Aries (c. 2002), REMUS (c. 2001–present) and Odyssey IV (2009–present).

Figure 2. AUVs past and present – NPS Phoenix, top left [9], NPS ARIES, top center [10], MIT Odyssey IV, top right [11], NPS REMUS, bottom

The initial design of the REMUS underwater vehicle did not feature cross-body thrusters and was instead controlled by a main propeller astern and a cruciform series of control fins. Prestero [12] studied this vehicle and proposed both non-linear and linear models for motions in all six degrees-of-freedom based on rigid-body Newtonian physics; that is:

$$\sum \vec{F} = m \cdot \vec{a} \tag{1}$$

$$\sum M = I \cdot \vec{\omega} \tag{2}$$

Model linearization is standard and provides a simple way to de-couple the otherwise highly non-linear equations of motion. The key tenet to this solution is its reliance on

small motions and small changes in the system dynamics; thereby eliminating several non-linear cross terms, keeping damping terms quadratic, and diagonalizing the mass and inertia tensors. Furthermore, restricting the model to small perturbations allows the matrix of Coriolis terms to be neglected.

Prestero did voluminous work in determining the exact parameters and coefficients of the original REMUS vehicle in operation; necessary for complete modeling of the vehicle in all six degrees-of-freedom. The values were determined analytically using several methods and then compared to data determined from experiments using the actual REMUS vehicle in the tow-tank. While several of the coefficients, including fin lift coefficients and forces, will remain close to the original values; the current evolution of the REMUS vehicle will have several changes to the added mass coefficients; as several of the principle dimensions are significantly larger. This thesis will utilize several of the same methods in determining the hydrodynamic coefficients and parameters pertaining to the enhanced version of the REMUS vehicle, using the original parameters determined in [12] as a baseline for comparison.

Fodrea [13] focused on utilizing forward-looking sonar in path planning and object avoidance maneuvers, using a REMUS vehicle of the same series as Prestero [12]. This problem has been under research since the advent of the autonomous underwater vehicle [13] as path planning and object avoidance are critical to mission success and vehicle longevity. The work proposed a multi-variable sliding mode controller (SMC), particularly useful in linear systems, as the governing control method for the line-of-sight guidance algorithms. The sliding mode controller provides a robust control system, advantageous to autonomous vehicles in the underwater environment. Fodrea reduced the system to two-dimensions (*x*-*y* plane only). The line-of-sight guidance algorithm functions by attempting to drive the heading error to zero:

$$\tilde{\psi}_{LOS} = \psi_{track}(t) - \psi(t) \tag{3}$$

where

$$\psi_{track}(t) = \tan^{-1}\left(\frac{y_{wpt(i)}(t) - y(t)}{x_{wpt(i)}(t) - x(t)}\right) \tag{4}$$

The work resulted in a very responsive controller, allowing the REMUS vehicle to regain desired track immediately after avoiding an object [13]. Crucial to this was the design of the weighting functions for bearing and range. The forward-looking sonar provides a very specific cone of view, and its accuracy is highly subject to the speed of the vehicle. The weighting functions applied large ("heavy") values to objects close to the vehicle, decreasing in value as range and relative bearing from the centerline increased.

The thruster control problem in a shallow water environment has been investigated by Reidel [14] using the NPS Phoenix AUV. Riedel examined the effects of environmental disturbances (waves) on a low-speed vehicle, and developed a Disturbance Compensation Controller (DCC) to assist the NPS Phoenix AUV in maintaining station, or loitering, in a particular area of interest. The DCC employs an Extended Kalman Filter (EKF) to continuously update the estimated system states based on corrupted ("noisy") measurements. This controller resulted in a new generalized approach to modeling underwater vehicles exposed to shallow water waves and currents, implementing direct fluid measurements to assimilate short-term wave-magnitude and direction information into a general prediction of sea disturbances.

Loitering control was examined further by Cooney [15], studying the MIT Odyssey IV AUV, which operated using azimuthing thrusters. The work presented a simple model for the unsteady thrust imparted by the azimuthing thrusters and developed a non-linear Model Predictive Controller to provide superior response when utilizing the thrusters in comparison to a standard Proportional-Integral-Derivative (PID) controller.

D. SCOPE OF THIS WORK

This work builds upon the foundation of REMUS knowledge previously presented, providing a robust vehicle simulator responsive in all 6 degrees-of-freedom. While the REMUS vehicle is highly responsive when using the cross-body thrusters, a valid simulation thereof remains unknown. This thesis develops a non-linear SIMULINK model in 6 degrees-of-freedom, modeling lift, drag, added mass, control forces and moments as an array of hydrodynamic coefficients. The non-linear model is then linearized to conduct analysis on lateral and vertical thruster effects on vehicle motion to

validate simulation results against actual REMUS vehicle in-water response and to develop a PID controller to minimize vehicle motions in the horizontal plane. The desired end-state is the implementation of this robust vehicle model and controller into the vehicle itself for further study.

Chapter II provides general background information on the history and development of the REMUS AUV. This will include comparative tables of physical and functional characteristics between the initial vehicle studied in [12] and [13] and the current vehicle in possession at NPS.

Chapter III presents the necessary vehicle and environmental assumptions, coordinate frame relations and equations of motion to model the REMUS vehicle in six degrees-of-freedom.

Chapter IV derives the necessary added mass matrix, hydrodynamic coefficients, and thruster force and torque relations utilizing several methods presented in [12].

Chapter V combines the equations of motion determined in Chapter III with the complete hydrodynamic coefficients presented in Chapter IV to obtain the full matrix representation of REMUS vehicle motion across all six degrees-of-freedom.

Chapter VI provides focused study on implementing control laws to eliminate vehicle instabilities as well as examining the full controllability of the vehicle. This chapter also provides an analysis of thruster effects on the linearized vehicle models.

Chapter VII discusses options to reduce error and provides possible avenues for continuing research.

THIS PAGE INTENTIONALLY LEFT BLANK

II. THE REMUS AUTONOMOUS UNDERWATER VEHICLE

A. HISTORY

Developed in 1994 by von Alt and associates of the Woods Hole Oceanographic Institution, the *R*emote *E*nvironmental *M*easuring UnitS, or REMUS, autonomous underwater vehicle designed to "provide researchers with a simple, low cost, rapid response capability" [16] to facilitate real-time oceanographic data collection in the marine environment. Although targeted at researchers, providing quick response to episodic events [16], the simple operational interface and relative low cost has significant appeal for military applications as well. Initial applications focused the development of REMUS vehicles to complement the Long Term Ecosystem Observatory (LEO-15), a cabled observatory system offshore from the Rutgers Marine Field Station near Tuckerton, New Jersey [17]. Multiple REMUS vehicles provide students and researchers continual access to underwater biological experimentation monitoring, ocean frontal system tracking, water column observation, sediment transport and bottom boundary layer growth and decay [16]. The capabilities have since expanded, paralleling the development of technology, and the REMUS is now used in a variety of missions, both civil and military, including [18]:

- Hydrographic surveys
- Mine Countermeasure (MCM) operations
- Environmental Monitoring
- Debris Field Mapping
- Search and Salvage operations
- Fishery operations
- Scientific sampling and mapping

B. THE REMUS SYSTEM PACKAGE

Available from Hydroid, Inc., the REMUS is provided in an all-inclusive package consisting of the REMUS vehicle, a ruggedized laptop with the REMUS GUI installed, power/data interface module, towfish transducer, a set of four navigation transponders and the REMUS Ranger. Figure 3 illustrates the REMUS 100 system package:

Figure 3. REMUS 100 System Package, from [18]

The design is a body-of-revolution, e.g. torpedo-shaped, based on a Myring hull profile [16], providing symmetry in the *x*-*y* and *x*-*z* planes. Table 1 provides the particulars for the original REMUS AUV (c. 2001):

Physical/Functional Area	Characteristic
Vehicle Diameter	7.5 [in]
Vehicle Length	62 [in]
Weight in air	80 [lbs]
External Ballast Weight	2.2 [lbs]
Operating Depth Range	10 [ft] to 60 [ft]
Transit Depth Limits	328 [ft]
Typical Search Area	875 [yds] x 1093 [yds]
Typical Transponder Range	1640 [yds]
Operational Temperature Range	+32 [°F] to +100 [°F]
Speed Range	0.5 [knots] to 5.6 [knots]
Maximum Operating Water Current	2 [knots]
Maximum Operating Sea State	Sea Sate 2
Battery	1 [kW-hr] internally rechargeable Lithium-ion
Endurance	20 [hrs] at 3 [knots]; 9 [hrs] at 5 [knots]

Table 1. Initial REMUS Functional and Physical Characteristics, from [13]

The design of the vehicle is modular, greatly easing upgrade implementation based on new commercial technology as available. Due to this, the current iteration of the REMUS AUV in possession at NPS is significantly larger and more capable, presented in Table 2.

Physical/Functional Area	Characteristic
Vehicle Diameter	7.5 [in]
Vehicle Length	107.25 [in]
Weight in air	145.60 [lbs]
External Ballast Weight	2.2 [lbs]
Operating Depth Range	10 [ft] to 60 [ft]
Transit Depth Limits	328 [ft]
Typical Search Area	875 [yds] x 1093 [yds]
Typical Transponder Range	1640 [yds]
Operational Temperature Range	+32 [°F] to +100 [°F]
Speed Range	0 [knots] to 5.6 [knots]
Maximum Operating Water Current	2 [knots]
Maximum Operating Sea State	Sea Sate 2
Battery	1 [kW-hr] internally rechargeable Lithium-ion
Endurance	20 [hrs] at 3 [knots]; 9 [hrs] at 5 [knots]

Table 2. Current REMUS Functional and Physical Characteristics

Of note, the length and weight of the vehicle vary significantly from its original counterpart. This is primarily due to the addition of the BlueView Forward Looking Sonar (FLS) package as well as the addition of the cross-body thruster package, both of which are shown in Figure 4.

Figure 4. BlueView Forward Looking Sonar Package

Figure 5. REMUS AUV with Cross-Body Thruster Package and an uncovered BlueView FLS

Other hardware and sensor upgrades available on the current NPS REMUS AUV are:

- Inertial Navigation System
- GPS Transponder
- Acoustic Modem

Due to the near doubling of critical vehicle parameters, particularly length and mass, significant deviations of hydrodynamic and hull-form coefficients from those presented in [12] and [13] are expected.

C. VEHICLE PROFILE

Derivation of all necessary hydrodynamic coefficients requires a complete analysis of the REMUS vehicle, including hull profile, centers of mass and buoyancy, mass distribution, and control fin parameters.

1. REMUS Hull Profile

The REMUS vehicle is based on the Myring hull profile equations that describe a body contour with minimal drag coefficient for a given length-to-diameter ratio [12]. The REMUS vehicle profile is based on the following modified parameters defined with an origin at the vehicle nose:

- *a*: the length of the nose section
- *b*: the length of the constant-radius center section
- *c*: the length of the tail section
- *d*: the maximum diameter
- *n*: an exponential parameter whose variation generates differing body shapes
- 2θ: the included tail angle

Nose shape is determined by the following modified semi-elliptical radius distribution [12]:

$$r(\Xi) = \left(\frac{1}{2}\right) d \left(1 - \left(\frac{\Xi + a_{offset} - a}{a}\right)^2\right)^{\frac{1}{n}} \tag{5}$$

where $r(\Xi)$ is the radius as a function of axial position measured normal to the vehicle centerline, Ξ is the axial position originating at the vehicle nose, a is the total nose length, and a_{offset} is the missing length of the nose.

The tail shape is determined using the following equation [12]:

$$r(\Xi) = \left(\frac{1}{2}\right)d - \left[\frac{3d}{2c^2} - \frac{\tan\theta}{c}\right](\Xi - l)^2 + \left[\frac{d}{c^3} - \frac{\tan\theta}{c^2}\right](\Xi - l_f)^3 \quad (6)$$

where the forward body length, l_f is defined as:

$$l_f = a + b - a_{offset} \quad (7)$$

and, once more, $r(\Xi)$ is the hull radius as a function of axial position and Ξ is the axial position. Figure 6 provides a relation of the parameters:

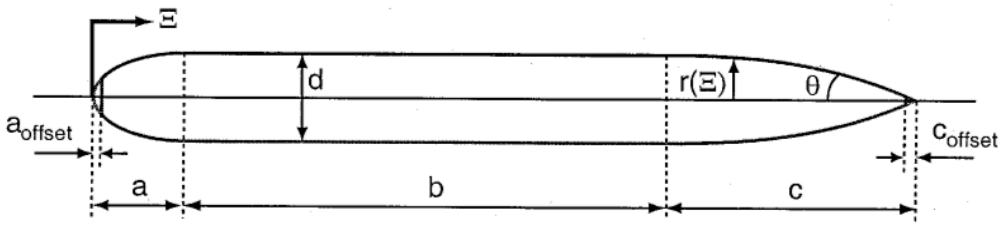

Figure 6. Myring Profile relationships, from [12]

Of note, the Myring profile includes a full tail length, while the REMUS vehicle itself has a snubbed tail, this difference is included as c_{offset}. This hull profile does not include any external appendages such as the control fins, sonar transducer, external ballast and GPS transceiver.

2. Centers of Mass and Buoyancy

Due to the modularity of the vehicle, the mass of the REMUS can vary significantly between missions. For the purposes of this research, however, the mass of the REMUS vehicle is presumed constant.

Parameter	Value	Units
x_{CG}	-1.35	[m]
y_{CG}	0.00	[m]
z_{CG}	-0.102	[m]

Table 3. Center of Gravity (datum at vehicle nose)

Similarly, the vehicle buoyancy is constant with a slight positive buoyancy of approximately 0.5 [kg] as a failsafe to force the vehicle to surface in the event of a casualty.

Parameter	Value	Units
x_{CB}	-1.36	[m]
y_{CB}	0.00	[m]
z_{CB}	0.00	[m]

Table 4. Center of Buoyancy (datum at vehicle nose)

3. Mass Distribution and Inertia Tensor

A critical assumption for the following hydrodynamic coefficient calculations involves determining the mass distribution and, in turn, the complete inertia tensor. As stated previously, the vehicle mass is unchanging. Traditionally, the mass distribution would sum the masses and locations of the individual vehicle components to provide a complete inertia tensor. As the vehicle components remain proprietary to their parent company, this work assumes a uniform mass distribution based on a uniform mass density of the vehicle. The mass density is determined as:

$$\rho_{REMUS} = \frac{m}{\nabla} \tag{8}$$

where m is the mass of the vehicle and ∇ is the volume of the vehicle defined by:

$$\nabla = \int_{x_t}^{x_{b_2}} \pi r\left(\Xi\right)^2 d\Xi \tag{9}$$

which is simply an integration of the instantaneous cross-sectional area of the vehicle over its length. Approximating the integral using Simpson's Rule yields the following:

$$\nabla \cong \left(\frac{l/99}{3}\right)\sum_{n=0}^{99}\begin{pmatrix} \pi r\left(\Xi_1\right)^2 + 4\left(\pi r\left(\Xi_2\right)^2\right) + 2\pi r\left(\Xi_3\right)^2 + \ldots \\ +2\left(\pi r\left(\Xi_{n-2}\right)^2\right) + 4\left(\pi r\left(\Xi_{n-1}\right)^2\right) + \pi r\left(\Xi_n\right)^2 \end{pmatrix} \tag{10}$$

where $\frac{l}{99}$ is the overall length sub-divided into 100 stations and $r\left(\Xi_n\right)$ is the vehicle radius at a given station.

The inertia tensor is defined as:

$$I = \begin{bmatrix} I_{xx} & -I_{xy} & -I_{xz} \\ -I_{yx} & I_{yy} & -I_{yz} \\ -I_{zx} & -I_{zy} & I_{zz} \end{bmatrix} \tag{11}$$

which, based on vehicle symmetry, can be reduced to the following:

$$I = \begin{bmatrix} I_{xx} & 0 & 0 \\ 0 & I_{yy} & -I_{yz} \\ 0 & -I_{zy} & I_{zz} \end{bmatrix} \tag{12}$$

The product of inertia, I_{yz}, is not neglected due to significant variations in vehicle shape in the forward and rear lengths. The general equations for remaining moments of inertia are:

$$I_{xx} = \int_V \left(y^2 + z^2\right) \rho_A dV = \sum_{n=1}^{K} m_n \left(y_n^2 + z_n^2\right) \tag{13}$$

$$I_{yy} = \int_V \left(x^2 + z^2\right) \rho_A dV = \sum_{n=1}^{K} m_n \left(x_n^2 + z_n^2\right) \tag{14}$$

$$I_{zz} = \int_V \left(x^2 + y^2\right) \rho_A dV = \sum_{n=1}^{K} m_n \left(x_n^2 + y_n^2\right) \tag{15}$$

$$I_{yz} = \int_V \left(yz\right) \rho_A dV = \int_V \left(zy\right) \rho_A dV = I_{zy} = \sum_{n=1}^{K} m_n \left(y_n z_n\right) \tag{16}$$

Applying previous relations regarding vehicle radius and once more invoking axial symmetry, the general equations become:

a. Moment of Inertia About the x-Axis

$$\begin{aligned} I_{xx} &= \int_V \left(y^2 + z^2\right) \rho_A dV = \sum_{n=1}^{K} m_n \left(y_n^2 + z_n^2\right) \\ I_{xx} &= \sum_{n=0}^{99} m_n \left(r\left(\Xi\right)_n^2 + r\left(\Xi\right)_n^2\right) = \sum_{n=0}^{99} m_n \left(2r\left(\Xi\right)_n^2\right) \end{aligned} \tag{17}$$

where n is the station number, $r(\Xi)_n$ is the hull radius at the specified station and m_n is the mass of the station defined by:

$$m_n = \rho_{REMUS}\left(\frac{l}{99}\right)\left(\pi r(\Xi)_n^2\right) \tag{18}$$

b. Moment of Inertia About the y- and z- Axes

Due to symmetry, the vehicle possesses identical moments of inertia about the y- and z- axes:

$$\begin{aligned} I_{yy} &= \int_V \left(x^2 + z^2\right)\rho_A dV = \sum_{n=1}^{K} m_n\left(x_n^2 + z_n^2\right) \\ I_{zz} &= \int_V \left(x^2 + y^2\right)\rho_A dV = \sum_{n=1}^{K} m_n\left(x_n^2 + y_n^2\right) \\ I_{yy} &= I_{zz} = \sum_{n=0}^{99} m_n\left(\Xi_n^2 + r(\Xi)_n^2\right) \end{aligned} \tag{19}$$

c. Product of Inertia Between the y- and z- Axes

$$\begin{aligned} I_{yz} &= \int_V (yz)\rho_A dV = \int_V (zy)\rho_A dV = I_{zy} = \sum_{n=1}^{K} m_n\left(y_n z_n\right) \\ I_{yz} &= I_{zy} = \sum_{n=0}^{99} m_n\left(r(\Xi)_n^2\right) \end{aligned} \tag{20}$$

d. Resulting Moments of Inertia

Parameter	Value	Units
I_{xx}	1.154	$\left[kg \cdot m^2\right]$
I_{yy}	34.70	$\left[kg \cdot m^2\right]$
I_{zz}	34.70	$\left[kg \cdot m^2\right]$
I_{yz}	0.5678	$\left[kg \cdot m^2\right]$

Table 5. Moments of Inertia (origin at vehicle half-length)

III. ELEMENTS OF THE GOVERNING EQUATIONS

A. INTRODUCTION

This chapter describes the assumptions and methods used to define the equations of motion, which model the motions experienced by the REMUS vehicle.

B. MODELING ASSUMPTIONS

The following assumptions apply to all aspects of this research:

1. Vehicle Dynamics Assumptions

- *The REMUS AUV can be modeled as a single rigid-body.* In other words, the mass distribution of the vehicle remains constant and rigid-body dynamics and kinematics are valid.
- *The REMUS AUV possesses constant mass.* The vehicle neither gains nor loses any mass during the course of its operations.
- *Control response time is instantaneous.* Change in control fin angle or thruster speed is immediate.
- *The REMUS AUV operates in a vehicle-centered coordinate frame.* The coordinate frame originates at the vehicle's center of buoyancy.

2. Environmental Assumptions

- *The REMUS AUV is submerged in a "safe harbor" environment.* That is, this model neglects wave effects and considers current effects as a linear additive.
- *Rotational effects of the earth are negligible.* Acceleration components of gravity on the center of mass are constant.
- *Forces acting on the REMUS vehicle are gravitational and inertial.* These forces are derived from hydrostatic, hydrodynamic and propulsive origins.

- *Fluid properties are constant.* That is, density (ρ), viscosity (μ), kinematic viscosity (v), temperature and salinity are all constant for seawater at 15.6˚C.
- *Local variances in the earth's gravitational field are ignored.* Acceleration due to gravity is constant and assumed to be g = 9.81 $\left[m/s^2 \right]$.

C. REFERENCE FRAME

The following standard SNAME notation [19] presented in Table 6 will be used to describe the degrees-of-freedom, forces, velocities, positions and angles:

Degree-of-Freedom (DOF)	Motion Description	Forces (F) and Moments (M)	Linear and Angular Velocities	Positions and Euler Angles
1	*Surge* – motions in the *x-direction.*	X	u	x
2	*Sway* – motions in the *y-direction.*	Y	v	y
3	*Heave* – motions in the *z-direction.*	Z	w	z
4	*Roll* – rotations about the *x-axis.*	K	p	ϕ
5	*Pitch* – rotations about the *y-axis.*	M	q	θ
6	*Yaw* – rotations about the *z-axis.*	N	r	ψ

Table 6. Notation used for the REMUS AUV

The first three DOFs describe the linear motion of the vehicle and the latter three describe the angular motion. It should be noted that, by convention, the positive *x*-direction is taken as forward, the positive *y*-direction is to the right, and the positive *z*-direction is down. This is commonly referred to as the *North-East-Down* [NED] coordinate frame. Furthermore, it is convenient to annotate the quantities in Table 6 into the following vectors:

$$\tau = [X, Y, Z, K, M, N]^T$$
$$\nu = [u, v, w, p, q, r]^T \quad (21)$$
$$x = [x, y, z, \phi, \theta, \psi]^T$$

To properly describe the motions of the REMUS vehicle, two orthogonal coordinate frames are required. The first is a global coordinate frame, usually considered to be earth-fixed. The second is a body-fixed coordinate frame, attached to the REMUS vehicle itself at the center of buoyancy (CB) and oriented to NED. Figure 7 shows the relation between the two coordinate frames and their respective forces, moments, velocities, and positions:

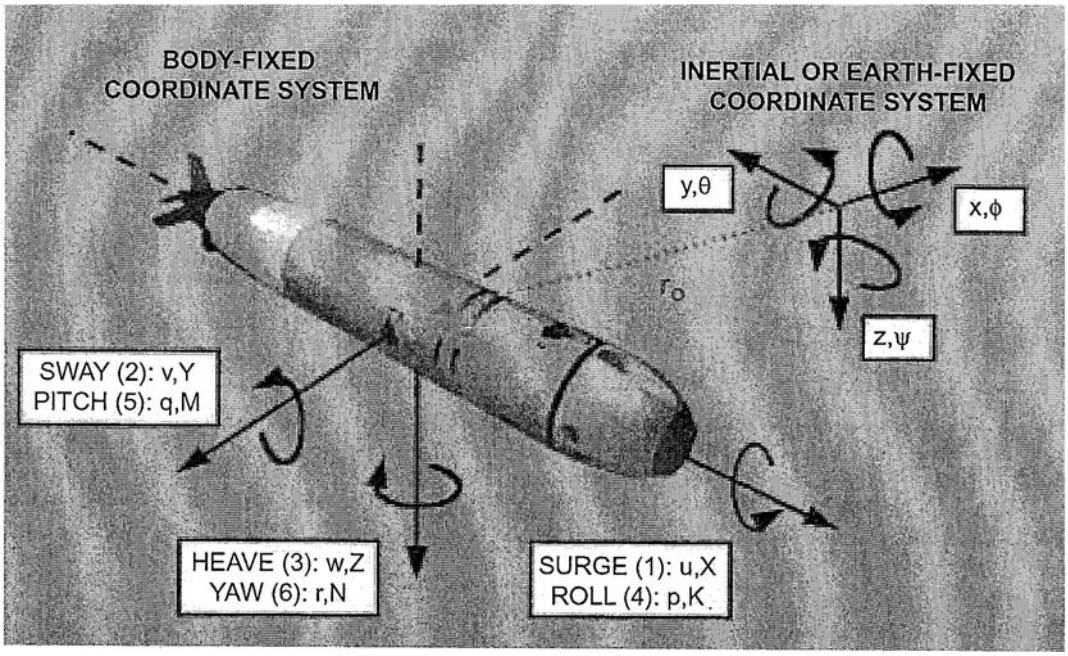

Figure 7. Coordinate Frame Relations, from [12]

Utilization of *Euler Angles* enables the transformation from one coordinate frame to another in the Cartesian coordinate system. The use of Euler angles requires each coordinate axis to be transformed individually. That is, the body must first be transformed about the *z*-axis, then transformed about the *y*-axis, and finally about the *x*-axis. The individual rotation matrices are:

$$R_{z,\psi} = \begin{bmatrix} \cos(\psi) & \sin(\psi) & 0 \\ -\sin(\psi) & \cos(\psi) & 0 \\ 0 & 0 & 1 \end{bmatrix} \tag{22}$$

$$R_{y,\theta} = \begin{bmatrix} \cos(\theta) & 0 & -\sin(\theta) \\ 0 & 1 & 0 \\ \sin(\theta) & 0 & \cos(\theta) \end{bmatrix} \tag{23}$$

$$R_{y,\theta} = \begin{bmatrix} 1 & 0 & 0 \\ 0 & \cos(\phi) & \sin(\phi) \\ 0 & \sin(\phi) & \cos(\phi) \end{bmatrix} \tag{24}$$

The total rotation matrix is the multiplication of the three:

$$R(\phi,\theta,\psi) = R_{x,\phi} R_{y,\theta} R_{z,\psi}$$

$$R(\phi,\theta,\psi) =$$

$$\begin{bmatrix} \cos(\psi)\cos(\theta) & -\sin(\psi)\cos(\phi)+\cos(\psi)\sin(\theta)\sin(\phi) & \sin(\psi)\cos(\phi)+\cos(\psi)\cos(\phi)\sin(\theta) \\ \sin(\psi)\cos(\theta) & \cos(\psi)\cos(\phi)+\sin(\psi)\sin(\theta)\sin(\phi) & -\cos(\psi)\sin(\phi)+\sin(\psi)\sin(\theta)\cos(\phi) \\ -\sin(\theta) & \cos(\theta)\sin(\phi) & \cos(\theta)\cos(\phi) \end{bmatrix}$$

$$\begin{bmatrix} u \\ v \\ w \end{bmatrix} = R(\phi,\theta,\psi) \begin{bmatrix} \dot{X} \\ \dot{Y} \\ \dot{Z} \end{bmatrix}$$

(25)

The above rotation matrix only enables the transformation of the body velocity vector to the global velocity vector; transformation of the angular velocities must be done as follows:

$$\begin{bmatrix} p \\ q \\ r \end{bmatrix} = R_{x,\phi} \begin{bmatrix} \dot{\phi} \\ 0 \\ 0 \end{bmatrix} + R_{x,\phi} R_{y,\theta} \begin{bmatrix} 0 \\ \dot{\theta} \\ 0 \end{bmatrix} + R_{x,\phi} R_{y,\theta} R_{z,\psi} \begin{bmatrix} 0 \\ 0 \\ \dot{\psi} \end{bmatrix}$$

$$\begin{bmatrix} p \\ q \\ r \end{bmatrix} = \begin{bmatrix} 1 & 0 & -\sin(\theta) \\ 0 & \cos(\phi) & \sin(\phi)\cos(\theta) \\ 0 & -\sin(\psi) & \cos(\phi)\cos(\theta) \end{bmatrix} \begin{bmatrix} \dot{\phi} \\ \dot{\theta} \\ \dot{\psi} \end{bmatrix} \tag{26}$$

Multiplying the angular velocity vector by the inverse combined rotation matrix yields angular accelerations:

$$\begin{bmatrix} \dot{\phi} \\ \dot{\theta} \\ \dot{\psi} \end{bmatrix} = \begin{bmatrix} 1 & \sin(\phi)\tan(\theta) & \cos(\phi)\tan(\theta) \\ 0 & \cos(\phi) & -\sin(\phi) \\ 0 & \frac{\sin(\phi)}{\cos(\theta)} & \frac{\cos(\phi)}{\cos(\theta)} \end{bmatrix} \begin{bmatrix} p \\ q \\ r \end{bmatrix} \tag{27}$$

It is important to recognize the singularity at pitch angles of $\theta = \pm 90°$. Generally speaking, underwater vehicles do not usually operate near these singularity points. The REMUS AUV, in particular, is designed to operate outside these singularities. Furthermore, the application of the cross-body thrusters provides any required direction change through both linear or angular forces and moments, instead of relying solely on angular moments applied by fin control surfaces.

D. EQUATIONS OF MOTION

The equations of motion are an extension of Newtonian physics:

$$\begin{aligned} \sum \vec{F} &= m \cdot \vec{a} \\ \sum M &= I \cdot \vec{\omega} \end{aligned} \tag{28}$$

where

$$\begin{aligned} \sum F &= F_{hydrostatic} + F_{lift} + F_{drag} + F_{control} \\ \sum M &= M_{hydrostatic} + M_{lift} + M_{drag} + M_{control} \end{aligned} \tag{29}$$

providing a vector representation of the equations of motion:

$$\begin{aligned} M\dot{\nu} &= \tau \\ M &= M_{RB} + M_A \end{aligned} \tag{30}$$

where M_{RB} and M_A are the rigid-body and added mass matrices, respectively and M is the complete mass matrix.

1. Vehicle Dynamics

Recalling the assumptions made in Chapter III.B, the above vector representation is broken down into its respective degrees-of-freedom below:

$$X = m\left[\dot{u} - vr + wq - x_{CG}\left(q^2 + r^2\right) + y_{CG}\left(pq - \dot{r}\right) + z_{CG}\left(pr + \dot{q}\right)\right] \tag{31}$$

$$Y = m\left[\dot{v} - wp + ur - y_{CG}\left(r^2 + p^2\right) + z_{CG}\left(qr - \dot{p}\right) + x_{CG}\left(qp + \dot{r}\right)\right] \tag{32}$$

$$Z = m\left[\dot{w} - uq + vp - z_{CG}\left(p^2 + q^2\right) + x_{CG}\left(rp - \dot{q}\right) + y_{CG}\left(rq + \dot{p}\right)\right] \tag{33}$$

$$\begin{aligned} K = {} & I_{xx}\dot{p} + \left(I_{zz} - I_{yy}\right)qr - \left(\dot{r} + pq\right)I_{xz} + \left(r^2 - q^2\right)I_{yz} + \left(pr - \dot{q}\right)I_{xy} \\ & + m\left[y_{CG}\left(\dot{w} - uq + vp\right) - z_{CG}\left(\dot{v} - wp + ur\right)\right] \end{aligned} \tag{34}$$

$$\begin{aligned} M = {} & I_{yy}\dot{q} + \left(I_{xx} - I_{zz}\right)rp - \left(\dot{p} + qr\right)I_{xy} + \left(p^2 - r^2\right)I_{zx} + \left(qp - \dot{r}\right)I_{xy} \\ & + m\left[z_{CG}\left(\dot{u} - vr + wq\right) - x_{CG}\left(\dot{w} - uq + vp\right)\right] \end{aligned} \tag{35}$$

$$\begin{aligned} N = {} & I_{zz}\dot{r} + \left(I_{yy} - I_{xx}\right)pq - \left(\dot{q} + rp\right)I_{yz} + \left(q^2 - p^2\right)I_{xy} + \left(rq - \dot{p}\right)I_{zx} \\ & + m\left[x_{CG}\left(\dot{v} - wp + ur\right) - y_{CG}\left(\dot{u} - vr + wq\right)\right] \end{aligned} \tag{36}$$

where m is the vehicle mass and I_{ij} is the following complete inertia tensor:

$$I = \begin{bmatrix} I_{xx} & -I_{xy} & -I_{xz} \\ -I_{yx} & I_{yy} & -I_{yz} \\ -I_{zx} & -I_{zy} & I_{zz} \end{bmatrix} \tag{37}$$

The first three equations model the translational motions of the vehicle and the second three model the rotational motions. Recall that the origin of the body-fixed coordinate frame is located at the center of buoyancy, $CB = \begin{bmatrix} x_{CB} & y_{CB} & z_{CB} \end{bmatrix}^T$; as such, the equations neglect these zero-valued terms. Furthermore, recalling the assumption that the REMUS vehicle possesses two planes (*xy*- and *yz*-) of symmetry, the products of inertia I_{xy}, I_{yx}, I_{xz}, and I_{zx} are negligible, reducing the inertia tensor to:

$$I = \begin{bmatrix} I_{xx} & 0 & 0 \\ 0 & I_{yy} & -I_{yz} \\ 0 & -I_{zy} & I_{zz} \end{bmatrix} \tag{38}$$

This reduces the equations of motion to:

$$X = m\left[\dot{u} - vr + wq - x_{CG}\left(q^2 + r^2\right) + y_{CG}\left(pq - \dot{r}\right) + z_{CG}\left(pr + \dot{q}\right)\right] \tag{39}$$

$$Y = m\left[\dot{v} - wp + ur - y_{CG}\left(r^2 + p^2\right) + z_{CG}\left(qr - \dot{p}\right) + x_{CG}\left(qp + \dot{r}\right)\right] \tag{40}$$

$$Z = m\left[\dot{w} - uq + vp - z_{CG}\left(p^2 + q^2\right) + x_{CG}\left(rp - \dot{q}\right) + y_{CG}\left(rq + \dot{p}\right)\right] \tag{41}$$

$$K = I_{xx}\dot{p} + \left(I_{zz} - I_{yy}\right)qr + \left(r^2 - q^2\right)I_{yz} + m\left[y_{CG}\left(\dot{w} - uq + vp\right) - z_{CG}\left(\dot{v} - wp + ur\right)\right] \quad (42)$$

$$M = I_{yy}\dot{q} + \left(I_{xx} - I_{zz}\right)rp + \left(qp - \dot{r}\right)I_{xy} + m\left[z_{CG}\left(\dot{u} - vr + wq\right) - x_{CG}\left(\dot{w} - uq + vp\right)\right] \quad (43)$$

$$N = I_{zz}\dot{r} + \left(I_{yy} - I_{xx}\right)pq - \left(\dot{q} + rp\right)I_{yz} + m\left[x_{CG}\left(\dot{v} - wp + ur\right) - y_{CG}\left(\dot{u} - vr + wq\right)\right] \quad (44)$$

Based on vehicle symmetry, ballasting characteristics, and internal layout, variances in the location of y_{CG} are negligible. This further reduces the equations of motion to:

$$X = m\left[\dot{u} - vr + wq - x_{CG}\left(q^2 + r^2\right) + z_{CG}\left(pr + \dot{q}\right)\right] \quad (45)$$

$$Y = m\left[\dot{v} - wp + ur + z_{CG}\left(qr - \dot{p}\right) + x_{CG}\left(qp + \dot{r}\right)\right] \quad (46)$$

$$Z = m\left[\dot{w} - uq + vp - z_{CG}\left(p^2 + q^2\right) + x_{CG}\left(rp - \dot{q}\right)\right] \quad (47)$$

$$K = I_{xx}\dot{p} + \left(I_{zz} - I_{yy}\right)qr + \left(r^2 - q^2\right)I_{yz} - m\left[z_{CG}\left(\dot{v} - wp + ur\right)\right] \quad (48)$$

$$M = I_{yy}\dot{q} + \left(I_{xx} - I_{zz}\right)rp + \left(qp - \dot{r}\right)I_{xy} + m\left[z_{CG}\left(\dot{u} - vr + wq\right) - x_{CG}\left(\dot{w} - uq + vp\right)\right] \quad (49)$$

$$N = I_{zz}\dot{r} + \left(I_{yy} - I_{xx}\right)pq - \left(\dot{q} + rp\right)I_{yz} + m\left[x_{CG}\left(\dot{v} - wp + ur\right)\right] \quad (50)$$

2. Vehicle Mechanics

In the preceding equations of motion, the external forces and moments, described in Equations (45) through (50) are described in terms of vehicle coefficients. These coefficients are a combination of theoretical equations and empirical formulations. The actual coefficient values are derived in the following chapter.

THIS PAGE INTENTIONALLY LEFT BLANK

IV. COEFFICIENT DERIVATION

A. INTRODUCTION

This chapter derives the coefficients representing external forces and moments upon the REMUS vehicle. While the standardized reference frame [19] remains in use, the correlating coefficients will retain their respective dimensions to facilitate comparison between this work and Prestero [12], contrary to the standard conventions presented in [19].

B. ADDED MASS

A vehicle's added mass represents the mass of the water column opposing the vehicle's line of motion, and is greatly influenced by the shape of the vehicle. Typically, the REMUS vehicle normally travels along a longitudinal axis of motion, introducing added mass to the nose and body from surface friction. Its slender profile, however, yields a relatively small added-mass tensor in this direction. Application of the cross-body thrusters, however, induces a motion subjecting the vehicle's entire length to a more resistive added mass tensor. Fossen [20] provides the full added mass matrix for an asymmetric submerged body:

$$M_A = \begin{bmatrix} X_{\dot{u}} & X_{\dot{v}} & X_{\dot{w}} & X_{\dot{p}} & X_{\dot{q}} & X_{\dot{r}} \\ Y_{\dot{u}} & Y_{\dot{v}} & Y_{\dot{w}} & Y_{\dot{p}} & Y_{\dot{q}} & Y_{\dot{r}} \\ Z_{\dot{u}} & Z_{\dot{v}} & Z_{\dot{w}} & Z_{\dot{p}} & Z_{\dot{q}} & Z_{\dot{r}} \\ K_{\dot{u}} & K_{\dot{v}} & K_{\dot{w}} & K_{\dot{p}} & K_{\dot{q}} & K_{\dot{r}} \\ M_{\dot{u}} & M_{\dot{v}} & M_{\dot{w}} & M_{\dot{p}} & M_{\dot{q}} & M_{\dot{r}} \\ N_{\dot{u}} & N_{\dot{v}} & N_{\dot{w}} & N_{\dot{p}} & N_{\dot{q}} & N_{\dot{r}} \end{bmatrix} \tag{51}$$

Because the REMUS vehicle is symmetric in the *x*-*y* (top-bottom) and *x*-*z* (port-starboard) planes, the added mass matrix reduces to:

$$M_A = \begin{bmatrix} X_{\dot{u}} & 0 & 0 & 0 & 0 & 0 \\ 0 & Y_{\dot{v}} & 0 & 0 & 0 & Y_{\dot{r}} \\ 0 & 0 & Z_{\dot{w}} & 0 & Z_{\dot{q}} & 0 \\ 0 & 0 & 0 & K_{\dot{p}} & 0 & 0 \\ 0 & 0 & M_{\dot{w}} & 0 & M_{\dot{q}} & 0 \\ 0 & N_{\dot{v}} & 0 & 0 & 0 & N_{\dot{r}} \end{bmatrix} \tag{52}$$

Expansion of the vector equation for fluid kinetic energy, $T_A = \frac{1}{2} \nu^T M_A \nu$, yields:

$$2T_A = X_{\dot{u}} u^2 + v\left(Y_{\dot{v}} v + Y_{\dot{r}} r\right) + w\left(Z_{\dot{w}} w + Z_{\dot{q}} q\right) + K_{\dot{p}} p^2 + q\left(M_{\dot{w}} w + M_{\dot{q}} q\right) + r\left(N_{\dot{v}} v + N_{\dot{r}} r\right) \tag{53}$$

Considering Kirchoff's Equations in component form [20]:

$$\frac{d}{dt}\frac{\partial T_A}{\partial u} = r\frac{\partial T_A}{\partial v} - q\frac{\partial T_A}{\partial w} - X_A \tag{54}$$

$$\frac{d}{dt}\frac{\partial T_A}{\partial v} = p\frac{\partial T_A}{\partial w} - r\frac{\partial T_A}{\partial u} - Y_A \tag{55}$$

$$\frac{d}{dt}\frac{\partial T_A}{\partial w} = q\frac{\partial T_A}{\partial u} - p\frac{\partial T_A}{\partial v} - Z_A \tag{56}$$

$$\frac{d}{dt}\frac{\partial T_A}{\partial p} = w\frac{\partial T_A}{\partial v} - v\frac{\partial T_A}{\partial w} + r\frac{\partial T_A}{\partial q} - q\frac{\partial T_A}{\partial r} - K_A \tag{57}$$

$$\frac{d}{dt}\frac{\partial T_A}{\partial q} = u\frac{\partial T_A}{\partial w} - w\frac{\partial T_A}{\partial u} + p\frac{\partial T_A}{\partial r} - r\frac{\partial T_A}{\partial p} - M_A \tag{58}$$

$$\frac{d}{dt}\frac{\partial T_A}{\partial r} = v\frac{\partial T_A}{\partial u} - u\frac{\partial T_A}{\partial v} + q\frac{\partial T_A}{\partial p} - p\frac{\partial T_A}{\partial q} - N_A \tag{59}$$

Substitution of Equations (54) through (59) into Equation (53) yields the complete set of equations for added mass:

$$\begin{bmatrix} X_A \\ Y_A \\ Z_A \\ K_A \\ M_A \\ N_A \end{bmatrix} = \begin{bmatrix} X_{\dot{u}} u^2 + Z_{\dot{w}} wq + Z_{\dot{q}} q^2 - Y_{\dot{v}} vr - Y_{\dot{r}} r^2 \\ Y_{\dot{v}} \dot{v} + Y_{\dot{r}} \dot{r} + X_{\dot{u}} ur - Z_{\dot{w}} wp - Z_{\dot{p}} pq \\ Z_{\dot{w}} \dot{w} + Z_{\dot{q}} \dot{q} - X_{\dot{u}} uq + Y_{\dot{v}} vp + Y_{\dot{r}} rp \\ K_{\dot{p}} \dot{p} \\ M_{\dot{w}} \dot{w} + M_{\dot{q}} \dot{q} - \left(Z_{\dot{w}} - X_{\dot{u}}\right) uw - Y_{\dot{r}} vp + \left(K_{\dot{p}} - N_{\dot{r}}\right) rp - Z_{\dot{q}} uq \\ N_{\dot{v}} \dot{v} + N_{\dot{r}} \dot{r} - \left(X_{\dot{u}} - Y_{\dot{v}}\right) uv + Z_{\dot{q}} wp - \left(K_{\dot{p}} - M_{\dot{q}}\right) pq + Y_{\dot{r}} ur \end{bmatrix} \tag{60}$$

The remainder of this section provides a breakdown of the added mass coefficients.

1. Axial Added Mass

The calculation for axial added mass approximates the REMUS hull-form as an ellipse for which half the vehicle length, l, is the major axis and half the vehicle's maximum diameter, d_{max}, is the minor axis. Blevins [21] presents the following empirical formula for the axial added mass of an ellipsoid:

$$X_{\dot{u}} = -\frac{4\alpha\rho\pi}{3}\left(\frac{l}{2}\right)\left(\frac{d_{\max}}{2}\right)^2 \tag{61}$$

or

$$X_{\dot{u}} = -\frac{4\beta\rho\pi}{3}\left(\frac{d_{\max}}{2}\right)^3 \tag{62}$$

where ρ is the local fluid density and α and β are empirical parameters measured as a function of the vehicle length to diameter, l/d_{max}, ratio.

l/d	**α**	**β**
0.01	-	0.6348
0.1	6.148	0.6148
0.2	3.008	0.6016
0.4	1.428	0.5712
0.6	0.9078	0.5447
0.8	0.6514	0.5211
1.0	0.5000	0.5000
1.5	0.3038	0.4557
2.0	0.2100	0.4200
2.5	0.1563	0.3908
3.0	0.1220	0.3660
5.0	0.05912	0.2956
7.0	0.03585	0.2510
10.0	0.02071	0.2071
∞	0	-

Table 7. Added Mass Parameters α and β, from [21]

Figure 8 plots α and β as a function of l/d_{max}:

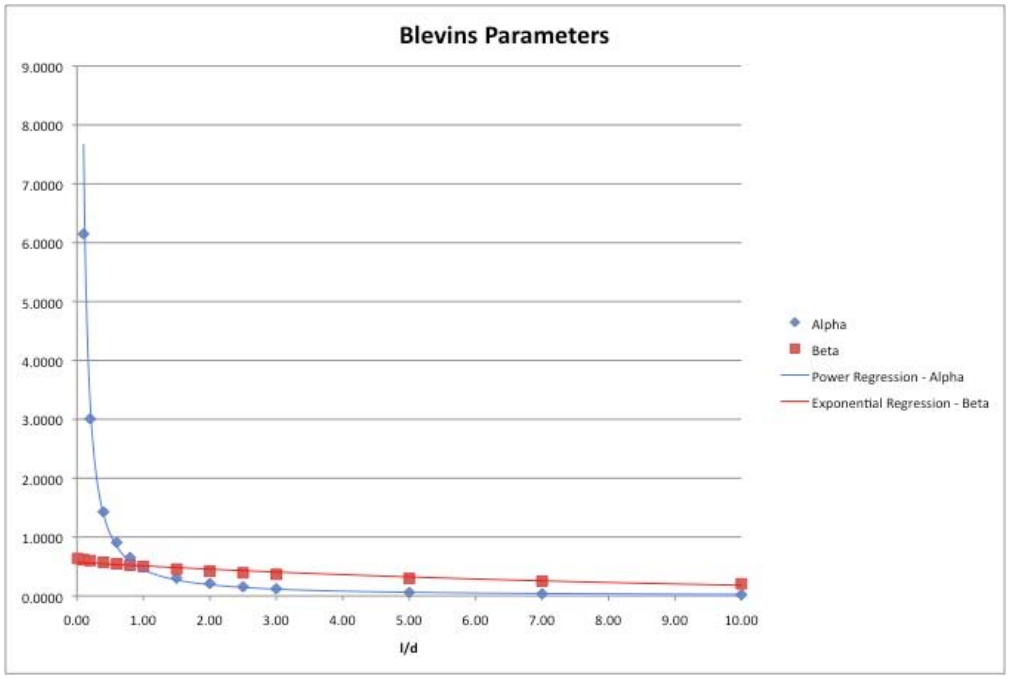

Figure 8. Blevins Parameters

Since $\frac{l}{d_{\max}} = 14.34$, which lies well outside the boundaries provided by Blevins, regression lines were plotted to extrapolate the required values for α and β yielding the following relations:

$$\alpha\left(\tfrac{l}{d_{\max}}\right) = 0.4466\left(\frac{l}{d_{\max}}\right)^{1.235}$$
$$\beta\left(\tfrac{l}{d_{\max}}\right) = 0.5720831e^{-0.1148249\left(\frac{l}{d_{\max}}\right)} \tag{63}$$

Appendix B tabulates all final coefficient values.

2. Cross-Flow Added Mass

Cross-flow added mass is computed using strip theory, a numerical integration technique. This term requires the combination of both cylindrical and cruciform hull cross sections. Blevins [21] indicates that the added mass per unit length of a cylindrical slice is:

$$m_a(\Xi) = \pi \rho r(\Xi)^2 \tag{64}$$

where ρ is the density of the surrounding fluid and $r(\Xi)$ defines the hull radius as a function of axial position. Blevins also defines the added mass of a circle with symmetric fins as:

$$m_{af}(\Xi) = \pi \rho a_f^2 \left(1 - \frac{r(\Xi)^2}{a_f^2} + \frac{r(\Xi)^4}{a_f^4}\right) \tag{65}$$

where a_f is the maximum fin height measured from the centerline of the vehicle.

Integrating the above two equations over the length of the vehicle yields the following equations for added mass:

$$Y_{\dot{v}} = -\int_{x_t}^{x_f} m_a(\Xi)\, d\Xi - \int_{x_f}^{x_{f2}} m_{af}(\Xi)\, d\Xi - \int_{x_{f2}}^{x_{b2}} m_a(\Xi)\, d\Xi \tag{66}$$

$$Y_{\dot{r}} = N_{\dot{v}} \tag{67}$$

$$Z_{\dot{w}} = Y_{\dot{v}} \tag{68}$$

$$Z_{\dot{q}} = M_{\dot{w}} \tag{69}$$

$$M_{\dot{w}} = \int_{x_t}^{x_f} \Xi \cdot m_a(\Xi)\, d\Xi - \int_{x_f}^{x_{f2}} \Xi \cdot m_a(\Xi)\, d\Xi - \int_{x_{f2}}^{x_{b2}} \Xi \cdot m_a(\Xi)\, d\Xi \tag{70}$$

$$M_{\dot{q}} = \int_{x_t}^{x_f} \Xi^2 \cdot m_a(\Xi)\, d\Xi - \int_{x_f}^{x_{f2}} \Xi^2 \cdot m_a(\Xi)\, d\Xi - \int_{x_{f2}}^{x_{b2}} \Xi^2 \cdot m_a(\Xi)\, d\Xi \tag{71}$$

$$N_{\dot{v}} = -M_{\dot{w}} \tag{72}$$

$$N_{\dot{r}} = M_{\dot{q}} \tag{73}$$

Appendix B describes and tabulates all final coefficient values. Table 13 in Appendix A provides the limits of integration.

3. Rolling Added Mass

The derivation of the rolling added mass term assumes that the cylindrical shape of the hull and any small protrusions thereof have no effect on the rolling added mass term. Based on this assumption, the only section of the vehicle contributing any appreciable rolling added mass is the tail section containing the vehicle's control surfaces (fins). Blevins [21] offers the following empirical formula for added mass of a rolling circle with multiple equally spaced fins:

$$K_{\dot{p}} = \int_{x_f}^{x_{f_2}} \frac{2}{\pi} \rho a^4 d\Xi \tag{74}$$

where *a* is the average fin height above the centerline of the vehicle. Table 13 and Table 14 in Appendix A provide the limits of integration and fin parameters, respectively.

4. Added Mass Cross-terms

The remaining added mass terms resulting from added mass coupling can be determined from calculations previously derived following the relationships presented in Table 8. The added mass cross-terms are grouped by row according to the respective degree of freedom and represent added mass along a degree of freedom due to coupling from off-axis velocities, both linear and angular.

$X_{wq} = Z_{\dot{w}}$	$X_{qq} = Z_{\dot{q}}$	$X_{vr} = -Y_{\dot{v}}$	$X_{rr} = -Y_{\dot{r}}$
$Y_{ur} = X_{\dot{u}}$	$Y_{wp} = -Z_{\dot{w}}$	$Y_{pq} = -Z_{\dot{q}}$	
$Z_{uq} = -X_{\dot{u}}$	$Z_{vp} = Y_{\dot{v}}$	$Z_{rp} = Y_{\dot{r}}$	
$M_{uwa} = -\left(Z_{\dot{w}} - X_{\dot{u}}\right)$	$M_{vp} = -Y_{\dot{r}}$	$M_{rp} = \left(K_{\dot{p}} - N_{\dot{r}}\right)$	$M_{uq} = -Z_{\dot{q}}$
$N_{uva} = -\left(X_{\dot{u}} - Y_{\dot{v}}\right)$	$N_{wp} = Z_{\dot{q}}$	$N_{pq} = -\left(K_{\dot{p}} - M_{\dot{q}}\right)$	$N_{ur} = Y_{\dot{r}}$

Table 8. Added Mass Cross-term Relations

The values for the added mass cross-terms are presented in Appendix B.

C. DRAG

Drag is a resistive force upon the vehicle that opposes the vehicle's line of motion, and is heavily influenced on the shape of the body, particularly the exposed area along the axis of motion. The governing equation for fluid drag is [22]:

$$F_D = \frac{1}{2} \rho C_D A V^2 \tag{75}$$

where F_D is the viscous drag force, ρ is the density of the surrounding fluid, C_D is the drag coefficient of the body, A is the area exposed along the axis motion, and V is the

body's velocity along the axis of motion. Since the viscous drag force always opposes the line of motion, it is necessary to consider the squared velocity term, V^2, as $V|V|$, resulting the following governing relation:

$$F_D = \frac{1}{2}\rho C_D A V|V| \tag{76}$$

yielding the appropriate sign.

1. Axial Drag

Axial drag is expressed by the following empirical relationship:

$$X_D = -\left(\frac{1}{2}\rho C_D A_F\right)u|u| \tag{77}$$

yielding the following non-linear axial drag coefficient:

$$X_{u|u|} = -\frac{1}{2}\rho C_D A_F \tag{78}$$

meaning

$$X_D = X_{u|u|}u|u| \tag{79}$$

where ρ is the density of the surrounding fluid, C_D is the vehicle's axial drag coefficient and A_F is the vehicle's frontal area.

Hoerner [23] presents the following empirical formula to calculate the axial drag coefficient, C_D:

$$C_D = 0.44\left(\frac{d}{l}\right) + 4C_f\left(\frac{l}{d}\right) + 4C_f\sqrt{\left(\frac{d}{l}\right)} \tag{80}$$

where the skin-friction drag coefficient, C_f, is determined using an approximation to the Schoenherr Equation [23]:

$$\frac{1}{\sqrt{C_f}} = 3.46\log(\mathrm{Re}) - 5.6 \tag{81}$$

or, more clearly:

$$C_f = \left(\frac{1}{3.46\log(\mathrm{Re}) - 5.6}\right)^2 \tag{82}$$

Hoerner states that the Schoenherr Equation is valid throughout the turbulent region of Reynolds numbers [23]:

$$\mathrm{Re} = \frac{Vl}{\nu} \tag{83}$$

where V is the vehicle's velocity, l is the length, and v is the kinematic viscosity of the surrounding fluid. Figure 9 shows the range of Reynolds numbers for the REMUS vehicle in seawater at 15.6˚C at speeds of: $0.25\left[m/s\right] \le V \le 2.57\left[m/s\right]$

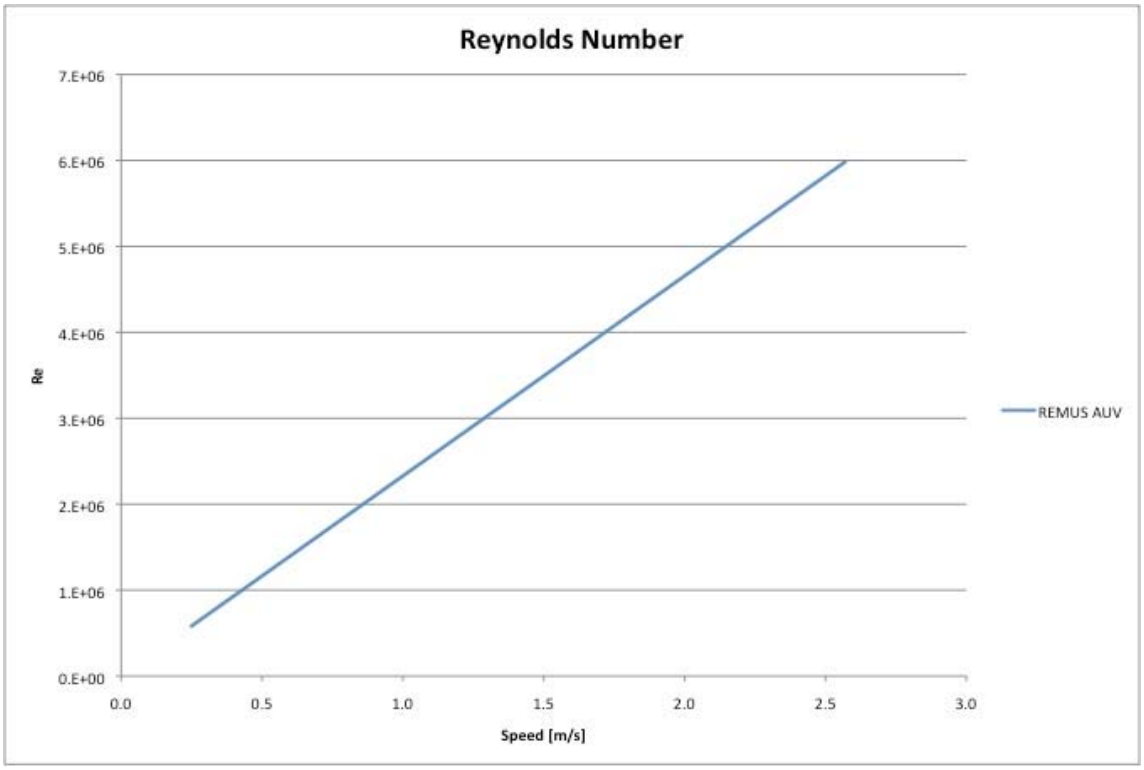

Figure 9. Reynolds Number Range for the REMUS AUV

The range of Reynolds numbers particular to the REMUS vehicle clearly fall within the standard values of the turbulent flow region, indicating the validity of using the approximation to the Schoenherr equation. Figure 10 and Figure 11 illustrate the trends for the drag coefficient, C_D, and the axial drag coefficient, $X_{u|u|}$, relative to the standard velocity range shown in Table 2.

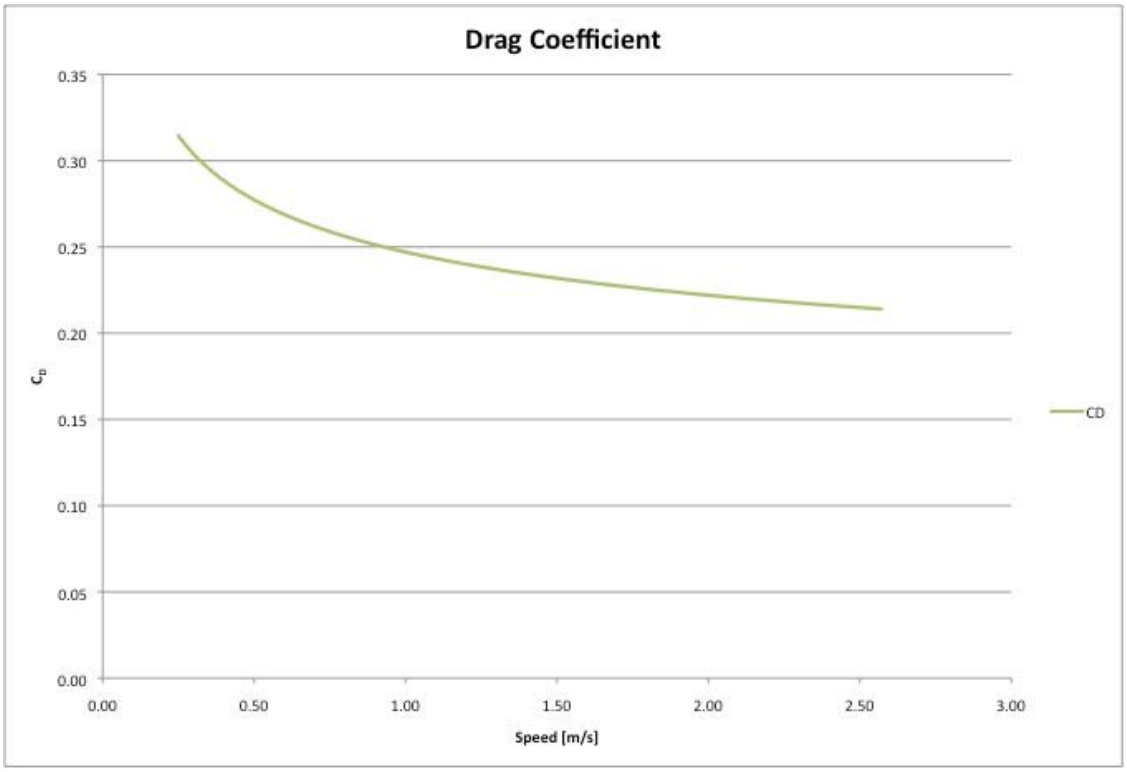

Figure 10. Drag Coefficient, C_D

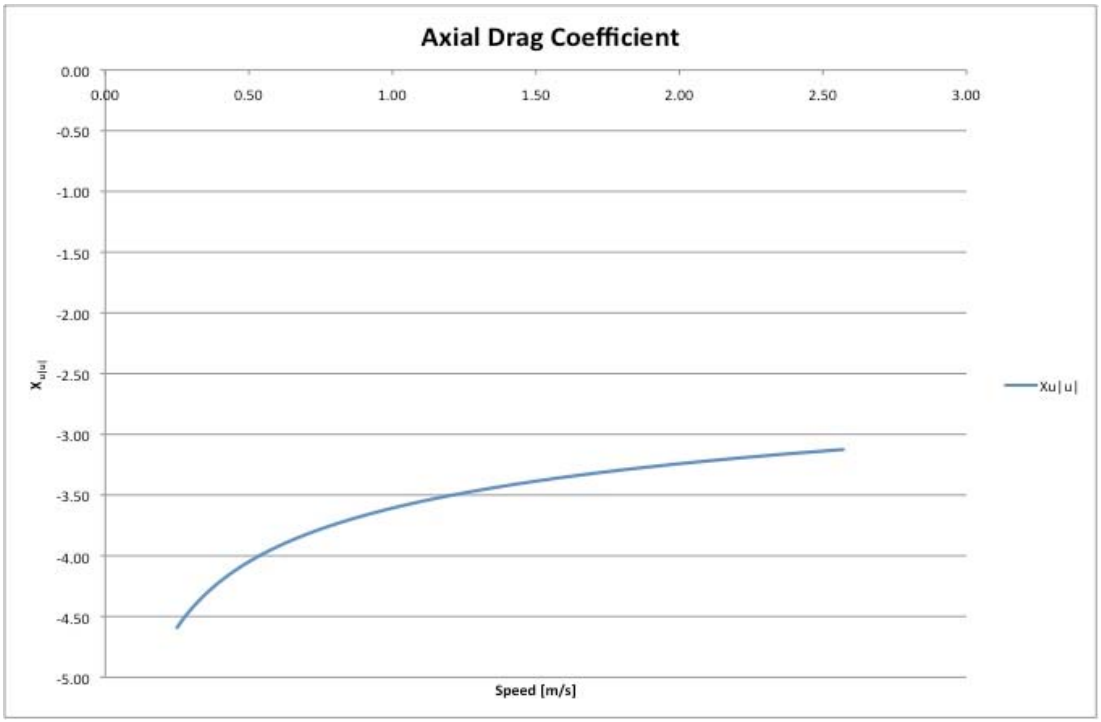

Figure 11. Axial Drag Coefficient, $X_{u|u|}$

The data trends follow an intuitive physical meaning – as velocity of the vehicle approaches $0\left[{}^{m}/_{s}\right]$, C_D approaches $+\infty$ and $X_{u|u|}$ approaches $-\infty$, consistent with the notion that a body at rest experiences an infinite drag resistance opposing its motion. Conversely, as the speed of the vehicle approaches infinity, the drag coefficients approach an asymptotic value.

Final values for both the skin-friction drag coefficient, C_f, the drag coefficient, C_D, and the axial drag coefficient, $X_{u|u|}$, are provided in Appendix B.

2. Cross-Flow Drag

Cross-flow drag is the summation of drag forces normal to the fluid flow; in the case of the REMUS vehicle, this includes both hull- and fin-induced cross-flow drag. As with axial drag, the shape of the body heavily influences the amount of cross-flow drag experienced. The method used to calculate cross-flow drag is analogous to the method used in Equations (66) through (73), however the accuracy when applied to viscous terms can be off by as much as 100% [12]. Inclusion of these terms, however, yields a fully defined model whose coefficients can be corrected with experimental data and observations at sea.

The non-linear cross-flow drag coefficients are calculated as follows:

$$Y_{v|v|} = Z_{w|w|} = -\frac{1}{2}\rho c_{dc}\int_{x_t}^{x_{b2}} 2r\left(\Xi\right)d\Xi - 2\left(\frac{1}{2}\rho S_{fin}c_{df}\right) \tag{84}$$

$$M_{w|w|} = -N_{v|v|} = \frac{1}{2}\rho c_{dc}\int_{x_t}^{x_{b2}} 2\Xi r\left(\Xi\right)d\Xi - 2x_{fin}\left(\frac{1}{2}\rho S_{fin}c_{df}\right) \tag{85}$$

$$Y_{r|r|} = -Z_{q|q|} = -\frac{1}{2}\rho c_{dc}\int_{x_t}^{x_{b2}} 2\Xi\left|\Xi\right| r\left(\Xi\right)d\Xi - 2x_{fin}\left|x_{fin}\right|\left(\frac{1}{2}\rho S_{fin}c_{df}\right) \tag{86}$$

$$M_{q|q|} = N_{r|r|} = -\frac{1}{2}\rho c_{dc}\int_{x_t}^{x_{b2}} 2\Xi^3 r\left(\Xi\right)d\Xi - 2x_{fin}^3\left(\frac{1}{2}\rho S_{fin}c_{df}\right) \tag{87}$$

where ρ is the density of the surrounding fluid, c_{dc} is the drag coefficient of a cylinder, Ξ is the axial position (shown in Figure 6 $r\left(\Xi\right)$ is the radius as a function of axial position (calculated in Equations (5) and (6)), x_{fin} is the axial fin-post location, S_{fin} is the fin planar area and c_{df} is the cross-flow drag coefficient of the fins.

The cylindrical cross-flow drag coefficient, c_{dc}, is estimated by [Hoerner] to be 1.1. The fin cross-flow drag coefficient, c_{df}, is derived using the following formula developed by Whicker and Fehlner [24]:

$$c_{df} = 0.1 + 0.7t \tag{88}$$

where t is the fin taper ratio.

Appendix B presents the final non-linear force and moment coefficients and Table 14 presents the REMUS fin parameters.

3. Rolling Drag

The rolling resistance of the REMUS vehicle will be approximated using the assumption that the primary contribution comes from the control fins, ignoring any other hull protrusions. This implies that:

$$F_{D_{roll}} = \left(Y_{vv_f} a_{avg}\right) a_{avg}^2 p|p| \tag{89}$$

where $F_{D_{roll}}$ is the drag force due to roll, Y_{vv_f} is the fin component of the vehicle cross-flow drag coefficient calculated by reducing the limits of integration from Equation (84) include only the hull section possessing fins, and r_{mean} is the mean fin height above the vehicle centerline. This defines the rolling drag coefficient as:

$$K_{p|p|} = Y_{vv_f} a_{avg}^3 \tag{90}$$

This method provides only a best estimate of rolling drag; experimental data would provide a better result.

D. LIFT

As a vehicle moves through a fluid at a specific angle of attack, it will experience lift as the flow separates around the vehicle and a pressure drop occurs. Depending on the angle of attack of the vehicle, this pressure drop will induce a pitching moment about the center of buoyancy and either force the vehicle to submerge deeper or begin to surface. In underwater vehicles, *body lift*, the lift force generated by the angle of attack and shape of the hull itself, is significant compared to the forces generated by the control

surfaces. Specifically, the body has a much larger area exposed to the flow. In aerial vehicles, on the other hand, the control surfaces are much larger, reducing the impact body lift has on the dynamics of the vehicle.

1. Body Lift Force

The body lift force is governed by the standard lift equation [25]:

$$F_L = \frac{1}{2}\rho C_L A V^2 \tag{91}$$

where F_L is the viscous lift force, ρ is the density of the surrounding fluid, C_L is the lift coefficient of the body, A is the area exposed along the axis of motion, and V is the body's velocity along the axis of motion. Nahon [26] proposes the following linear relationship between body lift coefficient and the vehicle's angle of attack:

$$C_{L_\beta} = \frac{2(k_2 - k_1)S_0}{\nabla^{2/3}} \tag{92}$$

where $(k_2\text{-}k_1)$ is an added mass factor determined by Munk [27], S_0 is the cross-sectional area of the body station where the flow ceases to be potential and ∇ is the hull volume. Munk's added mass factor, $(k_2\text{-}k_1)$, is a difference between transverse, k_2, and longitudinal, k_1, added masses for elongated surfaces of revolution. Table 9 provides Munk's data:

l/d	***k*$_1$ (Longitudinal)**	***k*$_2$ (Transverse)**	***k*$_2$ - *k*$_1$**
1.00	0.500	0.500	0.000
1.50	0.305	0.621	0.316
2.00	0.209	0.702	0.493
2.51	0.156	0.763	0.607
2.99	0.122	0.803	0.681
3.99	0.082	0.860	0.778
4.99	0.059	0.895	0.836
6.01	0.045	0.918	0.873
6.97	0.036	0.933	0.897
8.01	0.029	0.945	0.916
9.02	0.024	0.954	0.930
9.97	0.021	0.960	0.939
∞	0.000	1.000	1.000

Table 9. Munk's Added Mass Coefficients, from [27]

Use of Nahon's relation requires two assumptions based on the dimensions of the REMUS vehicle:

$$(k_2 - k_1) = 1.000 \tag{93}$$

$$S_0 = d_{max} \tag{94}$$

The first assumption is based on the fact that the REMUS vehicle has a considerably larger l/d_{max} ratio falling well outside Munk's empirical values. The second assumption dictates that the flow around the REMUS vehicle is steady through the initial contact with the vehicle's nose. Considering the smoothness of the hull-form at the nose, the uniformity of the diameter through the majority of the vehicle's length and the locations of various appendages, this assumption is reasonable. This implies the following relationship for the overall body lift force:

$$F_{L_{body}} = \frac{1}{2}\rho\left(\frac{2d_{max}}{\nabla^{2/3}}\right)AV^2 \tag{95}$$

meaning

$$Y_{uvl} = Z_{uwl} = \frac{1}{2}\rho\left(\frac{2d_{max}}{\nabla^{2/3}}\right)A \tag{96}$$

Appendix B tabulates all final coefficient values.

2. Body Lift Moment

Hoerner estimates the center of the lift force for an ellipsoid is "in the vicinity of 30% of the chord" [28]; in this case the chord is the overall length of the vehicle. This defines the center of pressure as:

$$x_{cp} = -0.70l \tag{97}$$

meaning that the body lift moment is:

$$M_{uvl} = N_{uwl} = \frac{1}{2}\rho\left(\frac{2d_{max}}{\nabla^{2/3}}\right)Ax_{cp} \tag{98}$$

Appendix B tabulates all final coefficient values.

3. Fin Lift Force

Attitude control, specifically rotations about the axes (i.e. *yaw*, *pitch*, and *roll*), are controlled in part by a pair each of rudders and stern planes arranged in a cruciform pattern at the aft end of the vehicle. Each control pair is slaved, that is individual rudders are not individually controlled. For vehicle control fins, the empirical formula for fin lift is given as [12]:

$$F_{L_{fin}} = \frac{1}{2}\rho C_{L_{fin}} S_{fin} \delta_e V_e^2 \tag{99}$$

where $F_{L_{fin}}$ is the lift force from the fin, $C_{L_{fin}}$ is the fin lift force coefficient, S_{fin} is the fin planform area, δ_e is the effective fin angle in radians, and V_e is the effective fin velocity. The fin lift coefficient, $C_{L_{fin}}$, is a function of the effective fin angle of attack, α. Hoerner [28] provides the following relation for the fin lift coefficient as a function of α:

$$C_{L_{fin}}(\alpha) = \frac{dC_{L_{fin}}}{d\alpha} = \left[\frac{1}{2\bar{\alpha}\pi} + \frac{1}{\pi(AR_e)}\right]^{-1} \tag{100}$$

where $\bar{\alpha}$ is a form factor for foil sections in undisturbed flow found by Hoerner to be "in the order of 0.9 [28]" and AR_e is the effective aspect ratio of the fin, given by the formula [12]:

$$AR_e = 2(AR) = 2\left(\frac{b_{fin}^2}{S_{fin}}\right) \tag{101}$$

where b_{fin} is the fin span.

Since the location of the control fins does not coincide directly with the origin of the vehicle coordinate system, the fins experience a slightly different effective velocity [12]:

$$u_{fin} = u + z_{fin} q - y_{fin} r \tag{102}$$

$$v_{fin} = v + x_{fin} r - z_{fin} p \tag{103}$$

$$w_{fin} = w + y_{fin} p - x_{fin} q \tag{104}$$

where u_{fin}, v_{fin}, and w_{fin} are the effective fin velocities and x_{fin}, y_{fin}, and z_{fin} are center-post locations of the control fins in the body-referenced coordinate system. Since the control

fins are placed in a standard cruciform pattern and because translational terms dominate, terms involving y_{fin} and z_{fin} are negligible.

The very nature of the control surfaces dictates that they experience an effective angle of attack relative to their orientation to the vehicle and the vehicle's orientation to the fluid.

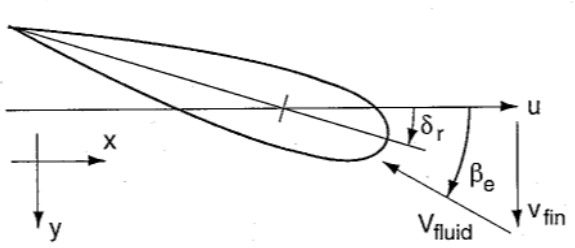

Figure 12. Effective Rudder Angle of Attack, from [12]

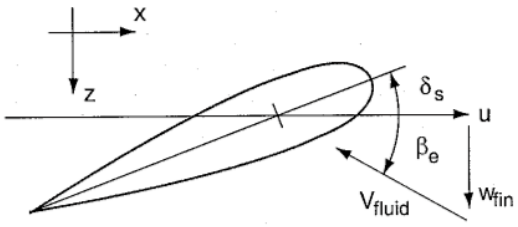

Figure 13. Effective Stern Plane Angle of Attack, from [12]

These effective angles of attack are expressed as [12]:

$$\delta_{r_{eff}} = \delta_r - \beta_{r_{eff}} \tag{105}$$

$$\delta_{s_{eff}} = \delta_s + \beta_{s_{eff}} \tag{106}$$

where δ_r and δ_s are the control fin angles in the body-referenced coordinate system, $\beta_{r_{eff}}$ and $\beta_{s_{eff}}$ are the effective angles of attack of the fin zero plane as shown in Figure 12 and Figure 13. Assuming small angles and carrying the assumptions made for relative fin velocities, these effective angles are expressed as [12]:

$$\beta_{r_{eff}} = \frac{v_{fin}}{u_{fin}} \approx \frac{\left(v + x_{fin} r\right)}{u} \tag{107}$$

$$\beta_{r_{eff}} = \frac{w_{fin}}{u_{fin}} \approx \frac{\left(w - x_{fin} q\right)}{u} \tag{108}$$

Substitution of Equations (100) through (108) into Equation (99) yields the following relationships governing fin lift:

$$Y_r = \frac{1}{2}\rho C_{L_{fin}} S_{fin}\left[u^2\delta_r - uv - x_{fin} ur\right] \tag{109}$$

$$Z_s = -\frac{1}{2}\rho C_{L_{fin}} S_{fin}\left[u^2\delta_s + uw - x_{fin} uq\right] \tag{110}$$

meaning that the fin lift coefficients are:

$$Y_{uu\delta r} = \frac{1}{2}\rho C_{L_{fin}} S_{fin} \tag{111}$$

$$Z_{uu\delta s} = -\frac{1}{2}\rho C_{L_{fin}} S_{fin} \tag{112}$$

$$Y_{ur_f} = -Z_{uw_f} = -\frac{1}{2}\rho C_{L_{fin}} S_{fin} x_{fin} \tag{113}$$

Appendix B tabulates all final coefficient values.

4. Fin Lift Moment

The fin lift moment is a simple extension of the fin lift force over the distance of the control fins from the body-referenced origin:

$$M_{L_{fin}} = F_{L_{fin}} x_{fin} \tag{114}$$

This results in the following equations for fin lift moments:

$$M_s = \frac{1}{2}\rho C_{L_{fin}} S_{fin}\left[u^2\delta_s + uw - x_{fin} uq\right] x_{fin} \tag{115}$$

$$Y_r = \frac{1}{2}\rho C_{L_{fin}} S_{fin}\left[u^2\delta_r - uv - x_{fin} ur\right] x_{fin} \tag{116}$$

further resulting in the following fin lift moment coefficients:

$$M_{uu\delta s} = \frac{1}{2}\rho C_{L_{fin}} S_{fin} x_{fin} \tag{117}$$

$$N_{uu\delta r} = \frac{1}{2}\rho C_{L_{fin}} S_{fin} x_{fin} \tag{118}$$

$$M_{uq_f} = -N_{ur_f} = -\frac{1}{2}\rho C_{L_{fin}} S_{fin} x^2{}_{fin} \tag{119}$$

Appendix B tabulates all final coefficient values.

E. HYDROSTATICS

The effects of weight and buoyancy impart the observed hydrostatic forces on the vehicle. Assuming *m* is the mass of the vehicle; requiring weight, $W = mg$, where *g* is the local acceleration due to gravity. Buoyancy, the restoring counter to weight is expressed as:

$$B = \rho g \nabla \tag{120}$$

where ρ is the local fluid density and ∇ is the volume of the vehicle. The REMUS AUV is designed to be slightly positively buoyant; a safety feature that guarantees eventual rise to the surface in the event of a malfunction. The combined hydrostatic forces and moments can be expressed as:

$$F_{HS} = f_{CG} - f_{CB} \tag{121}$$

$$M_{HS} = \left(r_{CG} \times f_{CG}\right) - \left(r_{CB} \times f_{CB}\right) \tag{122}$$

Applying the Euler angle transformations matrix, $R(\phi,\theta,\psi)$ derived in Equation (25) from Chapter III yields:

$$f_{CG} = R_{\phi\theta\psi}^{-1} \begin{bmatrix} 0 \\ 0 \\ W \end{bmatrix} \tag{123}$$

$$f_{CB} = R_{\phi\theta\psi}^{-1} \begin{bmatrix} 0 \\ 0 \\ B \end{bmatrix} \tag{124}$$

Expansion of this equation set yields the following set of hydrostatic forces and moments on the vehicle:

$$\begin{bmatrix} F_{HS} \\ M_{HS} \end{bmatrix} = \begin{bmatrix} X_{HS} \\ Y_{HS} \\ Z_{HS} \\ K_{HS} \\ M_{HS} \\ N_{HS} \end{bmatrix} = \begin{bmatrix} -(W-B)\sin\theta \\ (W-B)\cos\theta\sin\phi \\ (W-B)\cos\theta\cos\phi \\ -(y_{CG}W - y_{CB}B)\cos\theta\cos\phi - (z_{CG}W - z_{CB}B)\cos\theta\sin\phi \\ -(z_{CG}W - z_{CB}B)\sin\theta - (x_{CG}W - x_{CB}B)\cos\theta\cos\phi \\ -(x_{CG}W - x_{CB}B)\cos\theta\sin\phi - (y_{CG}W - y_{CB}B)\sin\theta \end{bmatrix} \tag{125}$$

F. PROPULSION MODEL

Propulsion for the REMUS vehicle is provided from 5 thrusters: a 3-bladed main propeller of diameter D_{prop} = 0.1143 $[m]$, and four cross-body thrusters of diameter $D_{thruster}$ = 0.0381 $[m]$. Modeling thrust for the REMUS vehicle requires a relationship between the input parameter of RPM and the output parameter of measured thrust. No governing empirical or analytical relationship between the two exists since thrust is a function several variables [29]:

$$F_T = f(\rho, D, V_A, g, n, p, \mu) \tag{126}$$

where

F_T = Thruster force
ρ = Density of the fluid
D = Diameter of the propeller
V_A = Speed of advance of the propeller
g = Acceleration due to gravity
n = Speed of rotation
p = Fluid pressure
μ = Viscosity of the fluid

Recalling the assumptions made in Chapter III, the relationship becomes simply:

$$F_T = f(n) \tag{127}$$

This is consistent with the control interface for the cross-body thrusters in the included REMUS GUI. The empirical relationship was determined analytically in a tow tank test at the Naval Postgraduate School.

1. Thruster Force Measurement

Suspending the REMUS vehicle from a crane and using a FUTEK USB Strain Gage, shown in Figure 14 provided accurate measurements of the forces imparted by the vertical thrusters.

Figure 14. FUTEK USB Strain Gage

The two thrusters were controlled in increments of 150 RPM or 3% of maximum RPM from 0 RPM to 5000 RPM. It is important to note that the pairs of thrusters are not slaved; that is, incremental change to one does not affect the other. This resulted in a slight lag as settings were altered. Measurements were collected after a lengthy period of stabilization to mitigate the effects of the un-slaved system and errors therein. Figure 15 plots the measured thrust as a function of rotational speed.

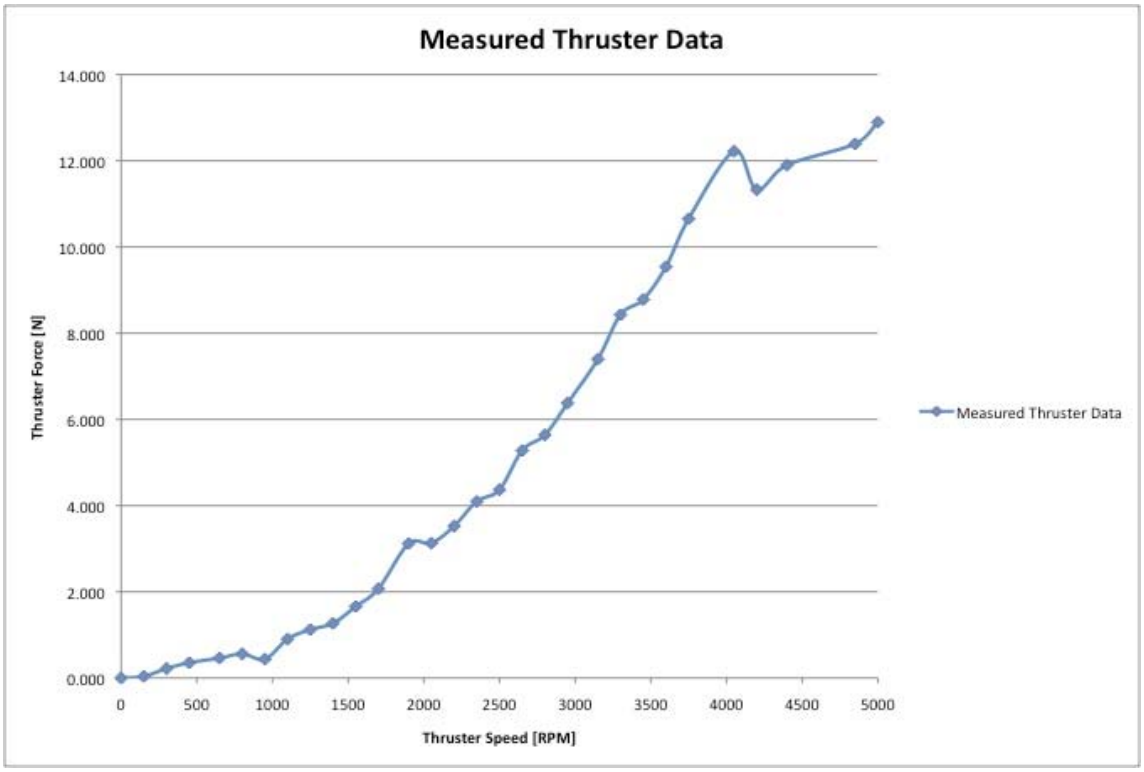

Figure 15. Measured Thruster Data

The measured data adheres closely to the following 4th order polynomial regression:

$$F_T = -\left(8.0712 \cdot 10^{-14} \cdot n^4\right) + \left(5.6674 \cdot 10^{-10} \cdot n^3\right) - \left(4.6335 \cdot 10^{-7} \cdot n^2\right) + \left(7.4831 \cdot 10^{-4} \cdot n\right) - \left(1.0795 \cdot 10^{-2}\right) \quad (128)$$

which is used in the REMUS model to provide an accurate assessment of thruster power from rotation speed input. This relation is assumed equivalent for all four cross-body thrusters, as all four thrusters are of identical size. Furthermore, since a polynomial regression is unbounded, the 4th order regression is only valid between the minimum and maximum rotation speeds.

2. Thruster Torque Calculation

Thruster torque is calculated using the following relation:

$$\mathrm{T} = F_T x_{loc} \quad (129)$$

where T is the calculated torque, F_T is the measured thrust, and x_{loc} is the location of each thruster relative to the vehicle's center of buoyancy. Plotting torque as a function of rotational speed results in Figure 16.

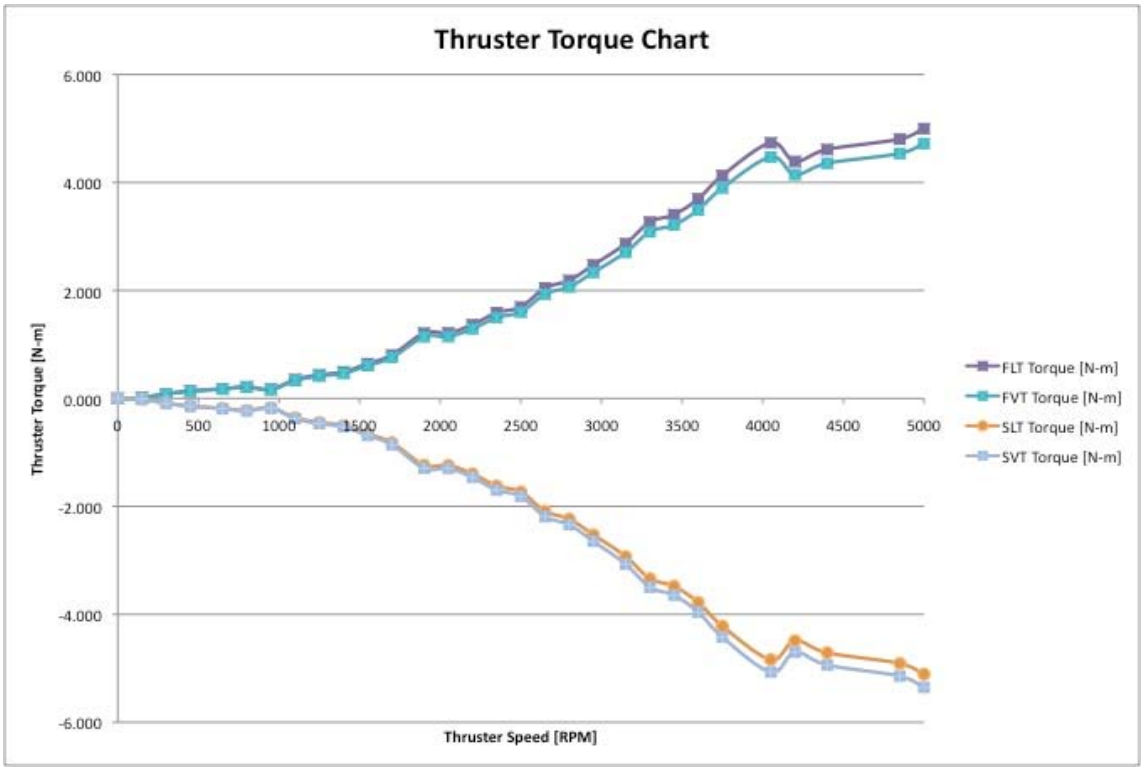

Figure 16. Thruster Torque Chart

The minor variations in torque are due to the differing location of each thruster relative to the center of buoyancy. Similar to the thruster data, the torque calculations adhere to a 4th order polynomial fit, resulting in the following set of equations:

$$T_{FLT} = -\left(3.128\cdot10^{-14}\cdot n^4\right)+\left(2.196\cdot10^{-10}\cdot n^3\right)-\left(1.795\cdot10^{-7}\cdot n^2\right)+\left(2.900\cdot10^{-4}\cdot n\right) -\left(4.183\cdot10^{-3}\right) \quad (130)$$

$$T_{FVT} = -\left(2.954\cdot10^{-14}\cdot n^4\right)+\left(2.074\cdot10^{-10}\cdot n^3\right)-\left(1.696\cdot10^{-7}\cdot n^2\right)+\left(2.739\cdot10^{-4}\cdot n\right) -\left(3.951\cdot10^{-3}\right) \quad (131)$$

$$T_{SLT} = \left(3.196\cdot10^{-14}\cdot n^4\right)-\left(2.244\cdot10^{-10}\cdot n^3\right)+\left(1.835\cdot10^{-7}\cdot n^2\right)-\left(2.963\cdot10^{-4}\cdot n\right) +\left(4.275\cdot10^{-3}\right) \quad (132)$$

$$T_{SVT} = \left(3.350 \cdot 10^{-14} \cdot n^4\right) - \left(2.352 \cdot 10^{-10} \cdot n^3\right) + \left(1.923 \cdot 10^{-7} \cdot n^2\right) - \left(3.106 \cdot 10^{-4} \cdot n\right) + \left(4.480 \cdot 10^{-3}\right) \quad (133)$$

Again, these equations are only valid between the minimum and maximum rotation speeds.

G. COMPLETE HYDRODYNAMIC TERMS

Description and tabulation of all non-linear force and moment coefficients derived in this chapter is provided in Appendix B.

V. COMPLETE MODEL AND TESTING

A. INTRODUCTION

This chapter combines the equations of motion discussed in Chapter III with the hydrodynamic coefficients derived in Chapter IV to provide a complete, six degree-of-freedom model for the REMUS vehicle. The SIMULINK model is adapted from the MATLAB model of the NPS Phoenix AUV provided in the Marine Systems Simulator Guidance, Navigation and Control (MSS GNC) toolkit [30].

B. COMBINED NON-LINEAR EQUATIONS OF MOTION

The combination of equations for rigid-body vehicle dynamics and the equations involving external forces and moments provide the complete set of non-linear equations governing the motion of the REMUS vehicle. These non-linear equations incorporate all the hydrodynamic coefficients and map the control input vector, $u = \begin{bmatrix} \delta_r & \delta_p & n_{FLT} & n_{SLT} & n_{FVT} & n_{SVT} & n \end{bmatrix}^T$, as a series of applied forces on the vehicle. The equations are presented below following the form of $\sum F_{body} = \sum F_{external}$ $\left(\text{or } \sum M_{body} = \sum M_{external}\right)$:

1. Surge

$$m\left[\dot{u} - vr + wq - x_{CG}\left(q^2 + r^2\right) + y_{CG}\left(pq - \dot{r}\right) + z_{CG}\left(pr + \dot{q}\right)\right] = X_{HS} + X_{u|u|}u|u| + X_{\dot{u}}\dot{u} + X_{wq}wq + X_{qq}q^2 + X_{vr}vr + X_{rr}r^2 + X_{prop} \quad (134)$$

2. Sway

$$m\left[\dot{v} - wp + ur - y_{CG}\left(r^2 + p^2\right) + z_{CG}\left(qr - \dot{p}\right) + x_{CG}\left(qp + \dot{r}\right)\right] = Y_{HS} + Y_{v|v|}v|v| + Y_{r|r|}r|r| + Y_{\dot{v}}\dot{v} + Y_{\dot{r}}\dot{r} + Y_{ur}ur + Y_{wp}wp + Y_{pq}pq + Y_{uv}uv + Y_{uu\delta_r}u^2\delta_r + Y_{prop} \quad (135)$$

3. Heave

$$m\left[\dot{w} - uq + vp - z_{CG}\left(p^2 + q^2\right) + x_{CG}\left(rp - \dot{q}\right) + y_{CG}\left(rq + \dot{p}\right)\right] = Z_{HS} + Z_{w|w|}w|w| + Z_{q|q|}q|q| + Z_{\dot{w}}\dot{w} + Z_{\dot{q}}\dot{q} + Z_{uw}uw + Z_{uq}uq + Z_{vp}vp + Z_{rp}rp + Z_{uu\delta_p}u^2\delta_p + Z_{prop} \quad (136)$$

4. Roll

$$I_{xx}\dot{p}+\left(I_{zz}-I_{yy}\right)qr+I_{yz}\left(r^2-q^2\right)+m\left[y_{CG}\left(\dot{w}-uq+vp\right)-z_{CG}\left(\dot{v}-wp+ur\right)\right]=K_{HS}+K_{p|p|}p\left|p\right|+K_{\dot{p}}\dot{p}+K_{prop} \quad (137)$$

5. Pitch

$$I_{yy}\dot{q}+\left(I_{xx}-I_{zz}\right)rp+I_{yz}\left(qp-\dot{r}\right)+m\left[z_{CG}\left(\dot{u}-vr+wq\right)-x_{CG}\left(\dot{w}-uq+vp\right)\right]=M_{HS}+M_{w|w|}w\left|w\right|+M_{q|q|}q\left|q\right|+M_{\dot{w}}\dot{w}+M_{\dot{q}}\dot{q}+M_{rp}rp+M_{uq}uq+M_{uw}uw+M_{vp}vp+M_{uu\delta_p}u^2\delta_p-M_{prop} \quad (138)$$

6. Yaw

$$I_{zz}\dot{r}+\left(I_{yy}-I_{xx}\right)pq+I_{yz}\left(\dot{q}+rp\right)+m\left[x_{CG}\left(\dot{v}-wp+ur\right)-y_{CG}\left(\dot{u}-vr+wq\right)\right]=N_{HS}+N_{v|v|}v\left|v\right|+N_{r|r|}r\left|r\right|+N_{\dot{v}}\dot{v}+N_{\dot{r}}\dot{r}+N_{uv}uv+N_{pq}pq+N_{ur}ur+N_{wp}wp+N_{uu\delta_r}u^2\delta_r-N_{prop} \quad (139)$$

Combining acceleration terms invokes an element of convenience for further manipulation into matrix form:

$$\left(m-X_{\dot{u}}\right)\dot{u}+mz_{CG}\dot{q}-my_{CG}\dot{r}=X_{HS}+X_{u|u|}u\left|u\right|+\left(X_{wq}-m\right)wq+\left(X_{qq}-mx_{CG}\right)q^2+\left(X_{vr}+m\right)vr+\left(X_{rr}+mx_{CG}\right)r^2-my_{CG}pq-mz_{CG}pr+X_{prop} \quad (140)$$

$$\left(m-Y_{\dot{v}}\right)\dot{v}-mz_{CG}\dot{p}+\left(mx_{CG}-Y_{\dot{r}}\right)\dot{r}=Y_{HS}+Y_{v|v|}v\left|v\right|+Y_{r|r|}r\left|r\right|+my_{CG}r^2+\left(Y_{ur}-m\right)ur+\left(Y_{wp}-m\right)wp+\left(Y_{pq}-mx_{CG}\right)pq+Y_{uv}uv+my_{CG}p^2+mz_{CG}qr+Y_{uu\delta_r}u^2\delta_r+Y_{prop} \quad (141)$$

$$\left(m-Z_{\dot{w}}\right)\dot{w}+my_{CG}\dot{p}-\left(mx_{CG}+Z_{\dot{q}}\right)\dot{q}=Z_{HS}+Z_{w|w|}w\left|w\right|+Z_{q|q|}q\left|q\right|+\left(Z_{uq}+m\right)uq+\left(Z_{vp}-m\right)vp+\left(Z_{rp}-mx_{CG}\right)rp+Z_{uw}uw+mz_{CG}\left(p^2+q^2\right)-my_{CG}rq+Z_{uu\delta_p}u^2\delta_p+Z_{prop} \quad (142)$$

$$-mz_{CG}\dot{v}+my_{CG}\dot{w}+\left(I_{xx}-K_{\dot{p}}\right)\dot{p}=K_{HS}+K_{p|p|}p\left|p\right|-\left(I_{zz}-I_{yy}\right)qr-I_{yz}\left(r^2-q^2\right)+my_{CG}\left(uq-vp\right)-mz_{CG}\left(wp-ur\right)+K_{prop} \quad (143)$$

$$
\begin{aligned}
mz_{Cg}\dot{u} - \left(mx_{CG} + M_{\dot{w}}\right)\dot{w} + \left(I_{yy} - M_{\dot{q}}\right)\dot{q} + I_{yz}\dot{r} = {} & M_{HS} + M_{w|w|}w|w| + M_{q|q|}q|q| \\
& + \left(M_{uq} - mx_{CG}\right)uq + \left(M_{vp} - mx_{CG}\right)vp \\
& + \left[M_{rp} - \left(I_{xx} - I_{zz}\right)\right]rp - I_{yz}qp \\
& + mz_{CG}\left(vr - wq\right) + M_{uw}uw \\
& + M_{uu\delta_p}u^2\delta_p + M_{prop}
\end{aligned}
\tag{144}
$$

$$
\begin{aligned}
-my_{CG}\dot{u} + \left(mx_{CG} - N_{\dot{v}}\right)\dot{v} + I_{yz}\dot{q} + \left(I_{zz} - N_{\dot{r}}\right)\dot{r} = {} & N_{HS} + N_{v|v|}v|v| + N_{r|r|}r|r| + \left(N_{ur} - mx_{CG}\right)ur \\
& + \left(N_{wp} + mx_{CG}\right)wp + \left[N_{pq} - \left(I_{yy} - I_{zz}\right)\right]pq \\
& + I_{yz}rp - my_{CG}\left(vr - wq\right) + N_{uv}uv + N_{uu\delta_r}u^2\delta_r \\
& + N_{prop}
\end{aligned}
\tag{145}
$$

Combining the coefficients and variables on the right-hand side of each equation into a $\left[\sum F \ \sum M\right]^T$ vector results in the following matrix form:

$$
\begin{bmatrix}
\left(m - X_{\dot{u}}\right) & 0 & 0 & 0 & mz_{CG} & -my_{CG} \\
0 & \left(m - Y_{\dot{v}}\right) & 0 & -mz_{CG} & 0 & \left(mx_{CG} - Y_{\dot{r}}\right) \\
0 & 0 & \left(m - Z_{\dot{w}}\right) & my_{CG} & \left(-mx_{CG} - Z_{\dot{q}}\right) & 0 \\
0 & -mz_{CG} & my_{CG} & \left(I_{xx} - K_{\dot{p}}\right) & 0 & 0 \\
mz_{CG} & 0 & \left(-mx_{CG} - M_{\dot{w}}\right) & 0 & \left(I_{yy} - M_{\dot{q}}\right) & -I_{yz} \\
-my_{CG} & \left(mx_{CG} - N_{\dot{v}}\right) & 0 & 0 & -I_{zy} & \left(I_{zz} - N_{\dot{r}}\right)
\end{bmatrix}
\begin{bmatrix}
\dot{u} \\ \dot{v} \\ \dot{w} \\ \dot{p} \\ \dot{q} \\ \dot{r}
\end{bmatrix}
=
\begin{bmatrix}
\sum X \\ \sum Y \\ \sum Z \\ \sum K \\ \sum M \\ \sum N
\end{bmatrix}
\tag{146}
$$

where the mass matrix is invertible, enabling solution of the acceleration vector directly using MATLAB/SIMULINK software.

C. IMPLEMENTATION INTO SIMULINK

The preceding matrix equations were implemented into the following SIMULINK system:

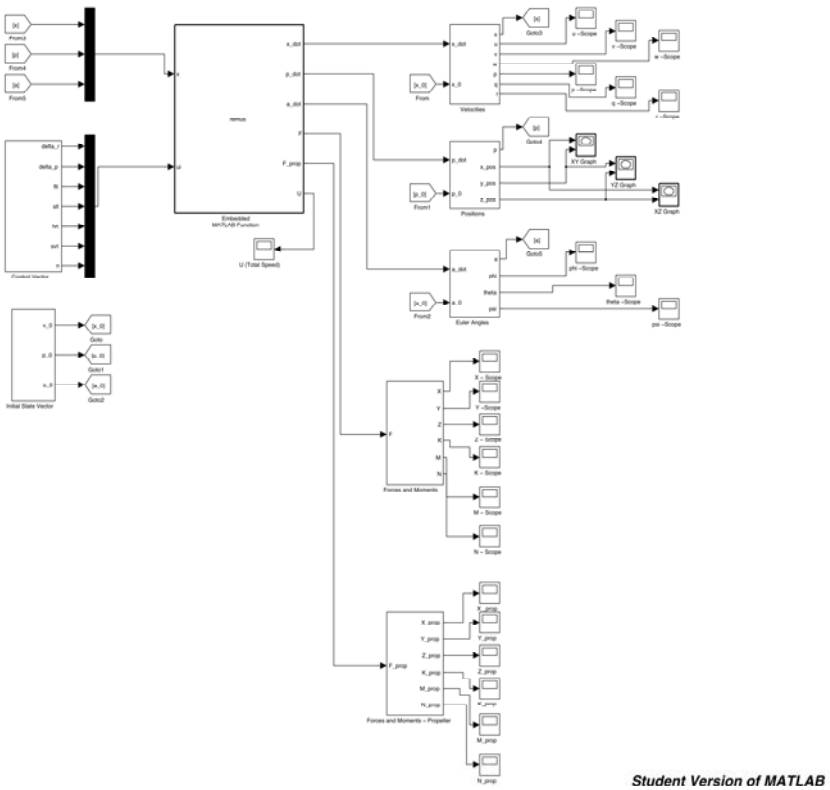

Figure 17. SIMULINK Block Diagram of the REMUS Vehicle

This vehicle model requires the following two inputs:

- *Vehicle Initial Conditions* – the initial state vector:

$$x = \begin{bmatrix} u & v & w & p & q & r & x_{pos} & y_{pos} & z_{pos} & \phi & \theta & \psi \end{bmatrix}^T \tag{147}$$

where u, v, w are measured in $\left[m/s \right]$, p, q, r are measured in $\left[\text{deg}/s \right]$, x, y, z are measured in $[m]$, and ϕ, θ, ψ are measured in $[\text{deg}]$.

- *Vehicle Control Inputs* – including rudder and plane pitch angles and thruster and main propeller rotation speeds:

$$u = \begin{bmatrix} \delta_r & \delta_p & n_{FLT} & n_{SLT} & n_{FVT} & n_{SVT} & n \end{bmatrix}^T \tag{148}$$

where δ_r, δ_p are rudder and plane commands in $[\text{deg}]$, $n_{FLT}, n_{SLT}, n_{FVT}, n_{SVT}, n$ are all thruster inputs in $[RPM]$.

The input vectors are executed in a feedback loop through the Embedded MATLAB Function *remus*, which contains all vehicle parameters and coefficients and solves the following equation:

$$\begin{bmatrix} \dot{u} \\ \dot{v} \\ \dot{w} \\ \dot{p} \\ \dot{q} \\ \dot{r} \end{bmatrix} = \begin{bmatrix} (m - X_{\dot{u}}) & 0 & 0 & 0 & mz_{CG} & -my_{CG} \\ 0 & (m - Y_{\dot{v}}) & 0 & -mz_{CG} & 0 & (mx_{CG} - Y_{\dot{r}}) \\ 0 & 0 & (m - Z_{\dot{w}}) & my_{CG} & (-mx_{CG} - Z_{\dot{q}}) & 0 \\ 0 & -mz_{CG} & my_{CG} & (I_{xx} - K_{\dot{p}}) & 0 & 0 \\ mz_{CG} & 0 & (-mx_{CG} - M_{\dot{w}}) & 0 & (I_{yy} - M_{\dot{q}}) & -I_{yz} \\ -my_{CG} & (mx_{CG} - N_{\dot{v}}) & 0 & 0 & -I_{zy} & (I_{zz} - N_{\dot{r}}) \end{bmatrix}^{-1} \begin{bmatrix} \sum X \\ \sum Y \\ \sum Z \\ \sum K \\ \sum M \\ \sum N \end{bmatrix} \tag{149}$$

where the acceleration vector is integrated directly, thereby obtaining the output state vector, as well as the output body force and thruster force vectors and total vehicle speed. The code for the Embedded MATLAB Function *remus* is presented in its entirety in Appendix C.

D. VEHICLE SIMULATIONS

The REMUS vehicle model was simulated using the following control vector input:

$$u = \begin{bmatrix} 0 & 0 & 2000 & -2000 & 0 & 0 & 0 \end{bmatrix}^T \tag{150}$$

resulting in the following vehicle motions:

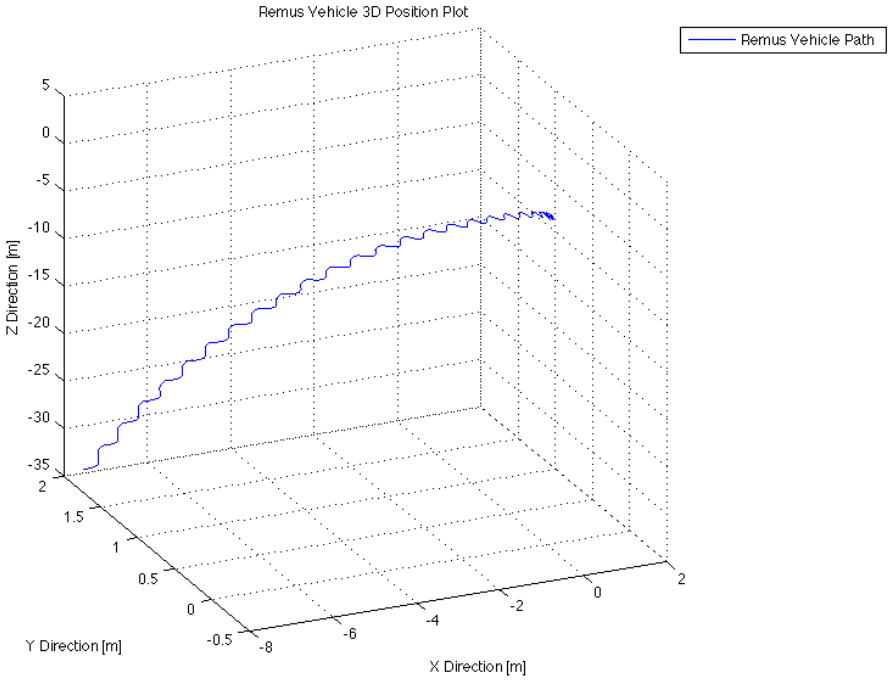

Figure 18. 3-D Position Plot, Standard Mission

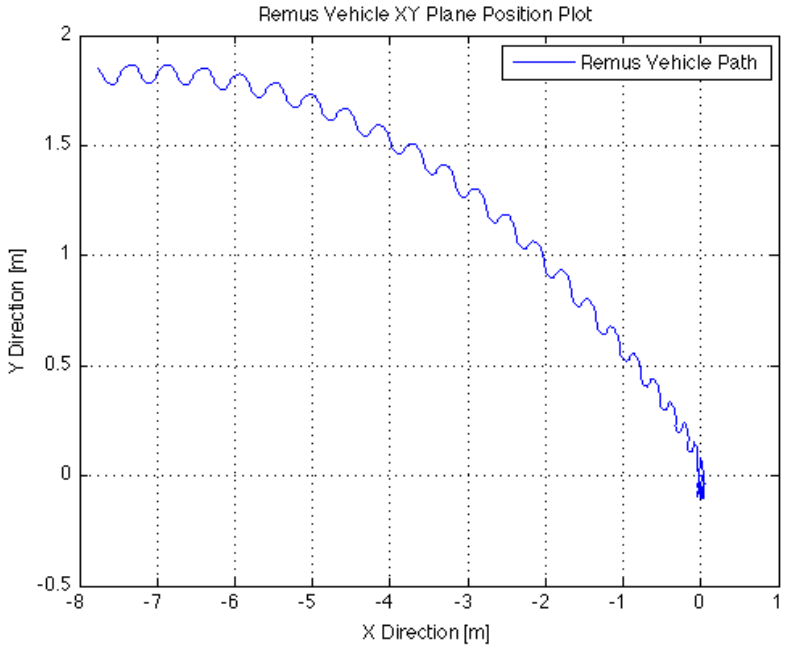

Figure 19. X-Y Plane Position Plot, Standard Mission

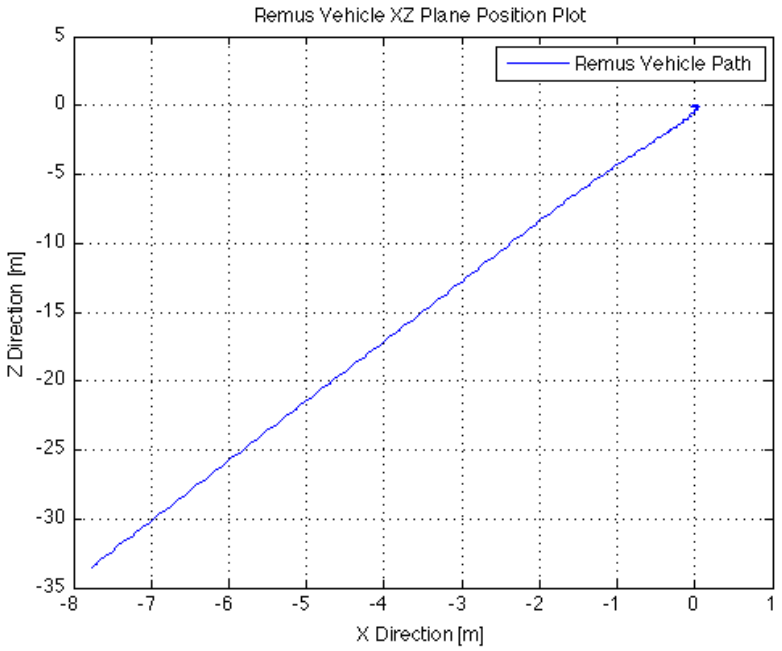

Figure 20. X-Z Plane Position Plot, Standard Mission

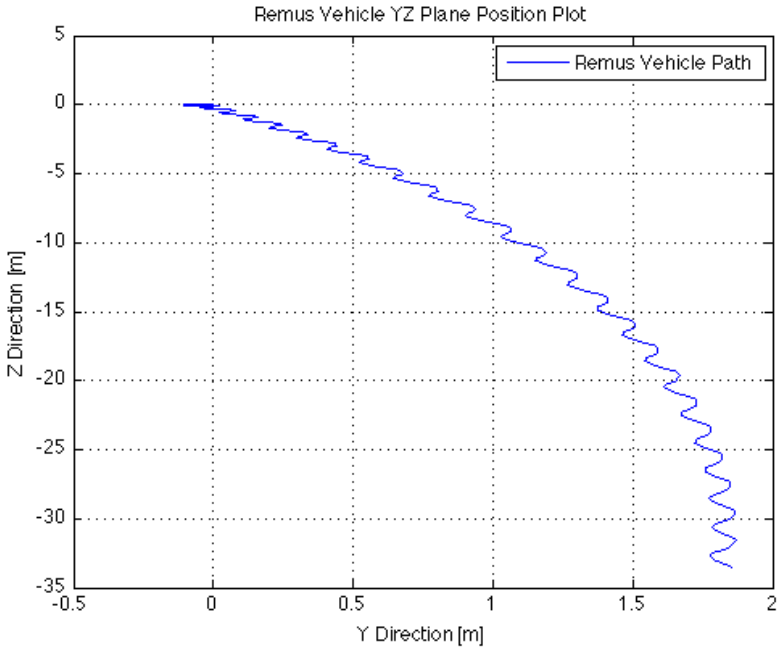

Figure 21. Y-Z Plane Position Plot, Standard Mission

Clearly, the vehicle is inherently unstable. The location of the cross-body thrusters relative to the center-point of the vehicle causes an unequal series of forces and moments about the body if equal thrust commands are applied, resulting in the sinusoidal oscillations along the path of advance. While not directly input, the path of advance is a result of these unequal force and moment distributions. Furthermore, in accordance with the standard North-East-Down frame of reference, the vehicle has a tendency to rise to the surface, denoted in the increasing negative values along the z-axis. This is a direct result of the inherent positive buoyancy of the REMUS vehicle in a standard operating environment.

Forcing the vehicle into neutral buoyancy, $W = B$, results in the following vehicle position plots:

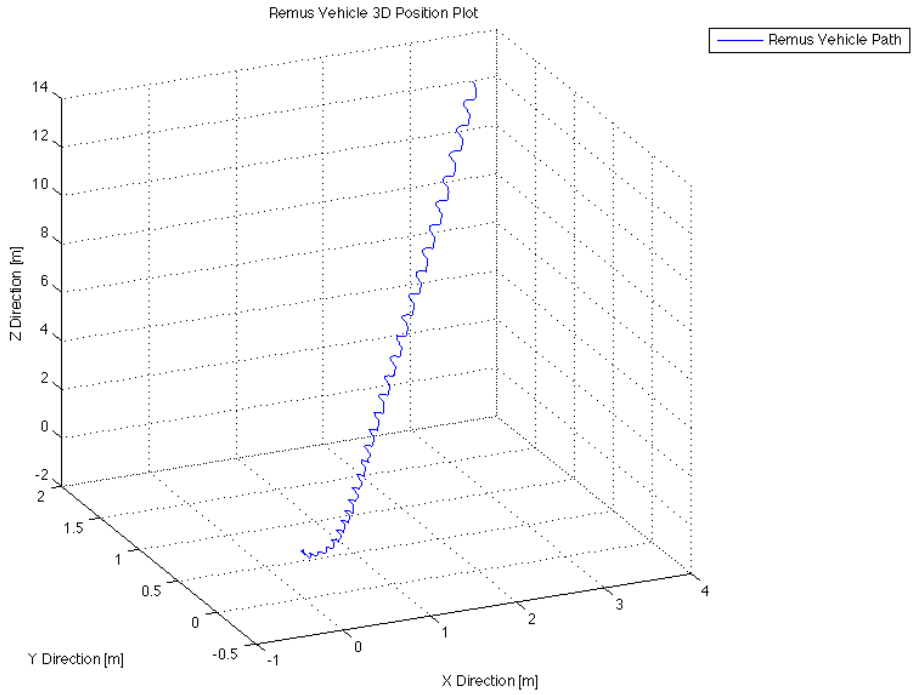

Figure 22. 3-D Position Plot, Neutral Buoyancy

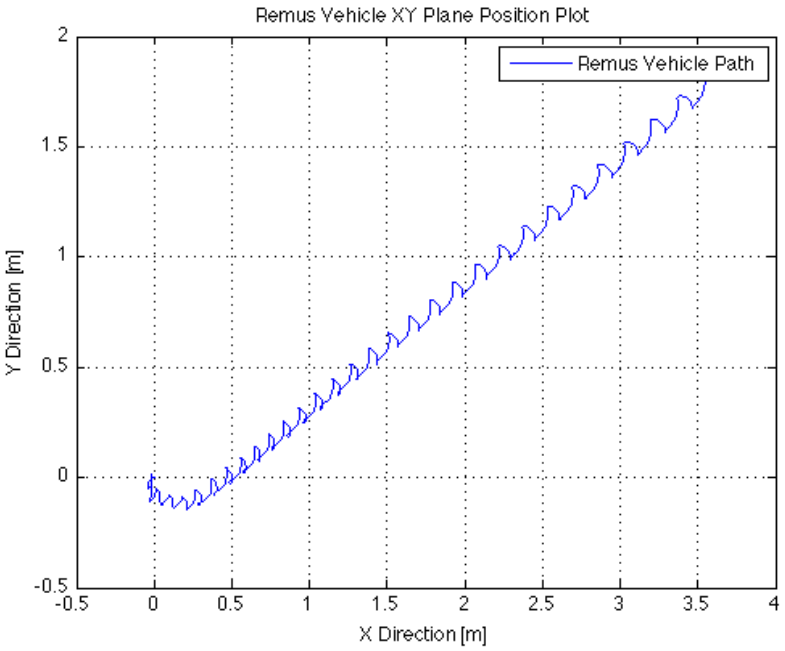

Figure 23. X-Y Plane, Neutral Buoyancy

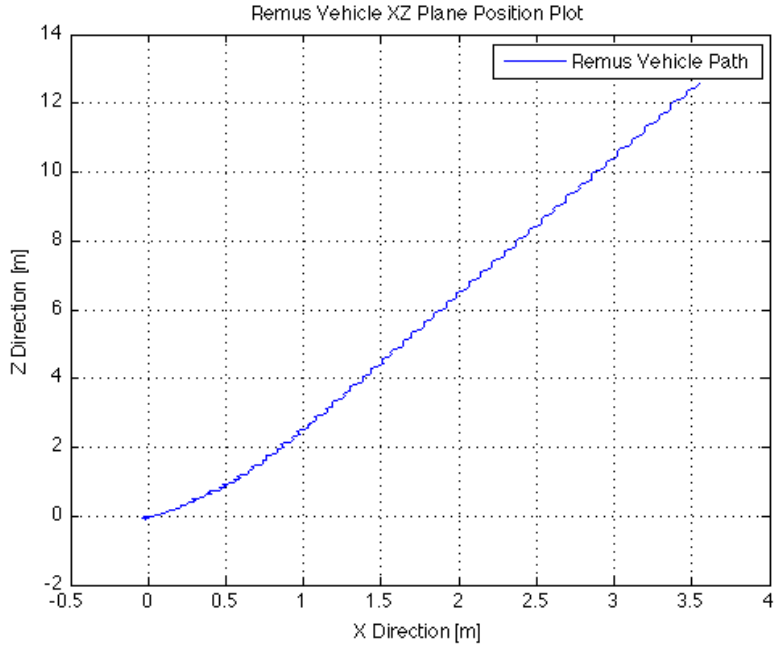

Figure 24. X-Z Plane, Neutral Buoyancy

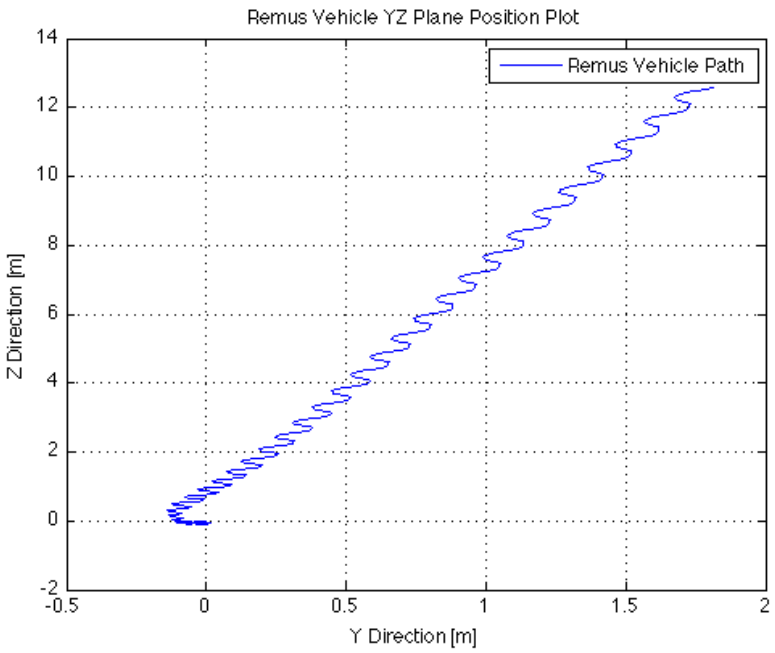

Figure 25. Y-Z Plane, Neutral Buoyancy

The oscillatory behavior remains; however, the vehicle tends to dive. This tendency is attributed to vehicle instability in roll. Implementation of a series of control algorithms is required to provide complete vehicle stability.

VI. CONTROL IMPLEMENTATION

A. INTRODUCTION

This chapter presents the implementation of a Proportional-Integral-Derivative (PID) controller to stabilize motions in yaw rate, *r*. PID controllers are widely used because they are generally applicable to most control systems and are particularly useful when a complete mathematical model of the plant is unknown [31].

The state space and thruster control models developed in Chapters IV and V provide a first order differentiable system resulting in simulation estimates on required lateral thruster inputs to minimize vehicle motions in the *x-y* plane. These estimates are then incorporated into the PID controller.

This chapter then discusses the validity of control all motions in the *x-y* plane, $u,\ v,\ r,\ \psi, x_{pos}, y_{pos}$, utilizing only the lateral cross-body thrusters to force rotation about the *z*-axis without deviation in the *x-y* plane.

B. PID CONTROL OF YAW RATE

A PID controller is a feedback mechanism that calculates the error between a desired operating point and the measured value. For yaw rate, $\dot{\psi}$, the error equation is:

$$\dot{\psi}_e(t) = \dot{\psi}_c - \dot{\psi}(t) \tag{151}$$

where $\dot{\psi}_e(t)$ is the error in yaw rate as a function of time, $\dot{\psi}_c$ is the constant commanded yaw rate and $\dot{\psi}(t)$ is the measured yaw rate as a function of time from the REMUS computer simulation. The general block diagram for a PID controller is presented in Figure 26.

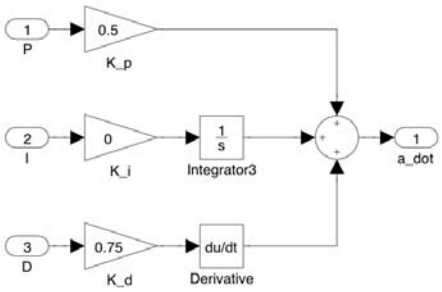

Figure 26. Yaw Rate PID Controller Block Diagram

In Figure 26, K_P, K_I, K_D are the proportional, integral and derivative gains, respectively. The values shown in Figure 26 were chosen via trial and error. In fact, what is shown in the figure is a Proportional-Derivative (PD) controller rather than a full PID controller. The input to the *P*, *I*, and *D* blocks is the difference between the commanded angular velocity and the angular velocity calculated through the REMUS vehicle model (i.e. the output of Equation (151)). The commanded angular velocity was set to $\dot{\psi}_c = 7.0\left[\,{}^{\deg}\!/_{s}\,\right]$, with the identical control input vector from Chapter V Section D and standard mission profile of slight positive buoyancy. Figures 27 through 31 present the results of simulation with a closed yaw-rate loop:

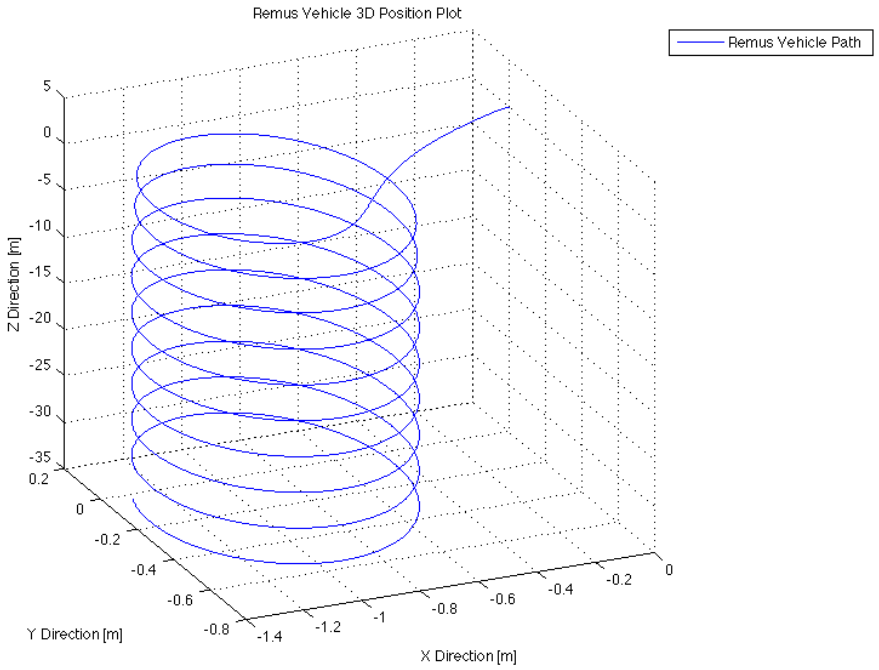

Figure 27. 3-D Position Plot, PID Control Implemented

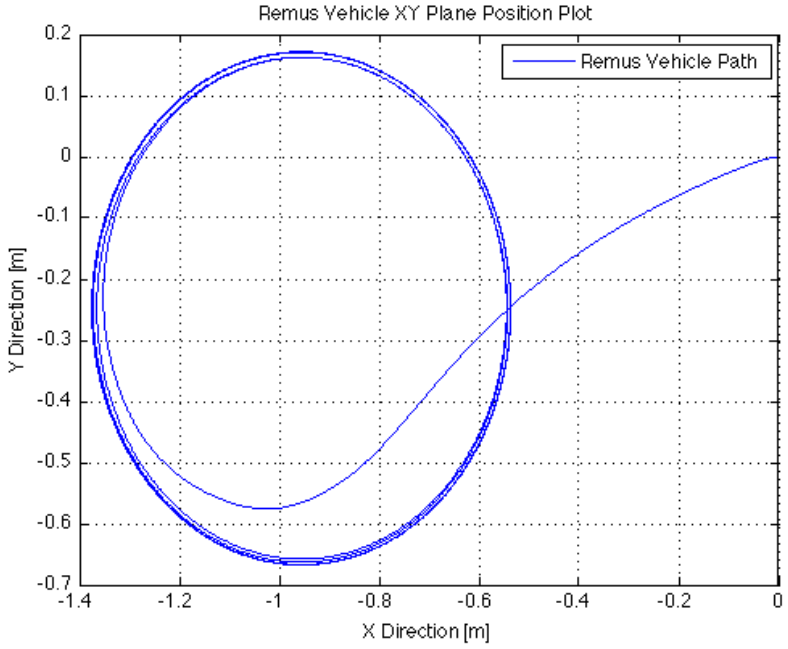

Figure 28. X-Y Plane Position Plot, PID Control Implemented

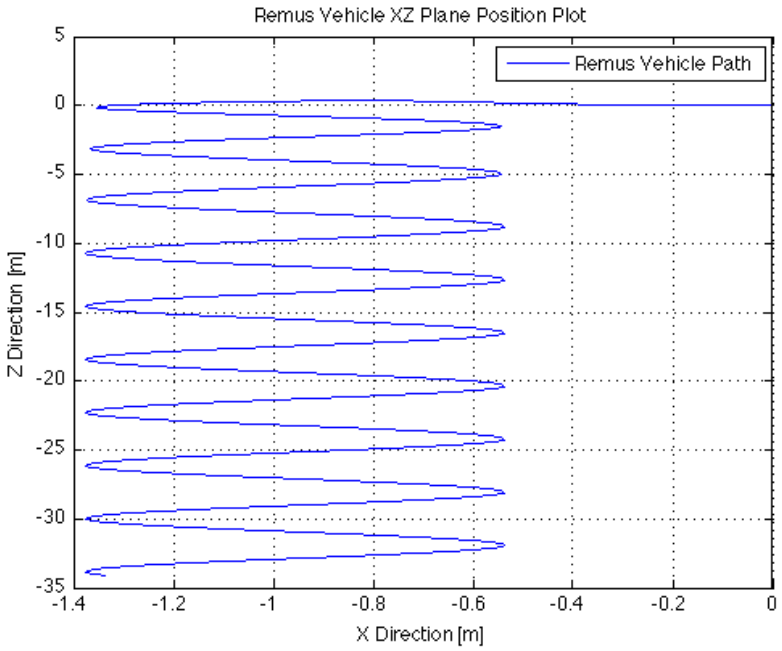

Figure 29. X-Z Plane Position Plot, PID Control Implemented

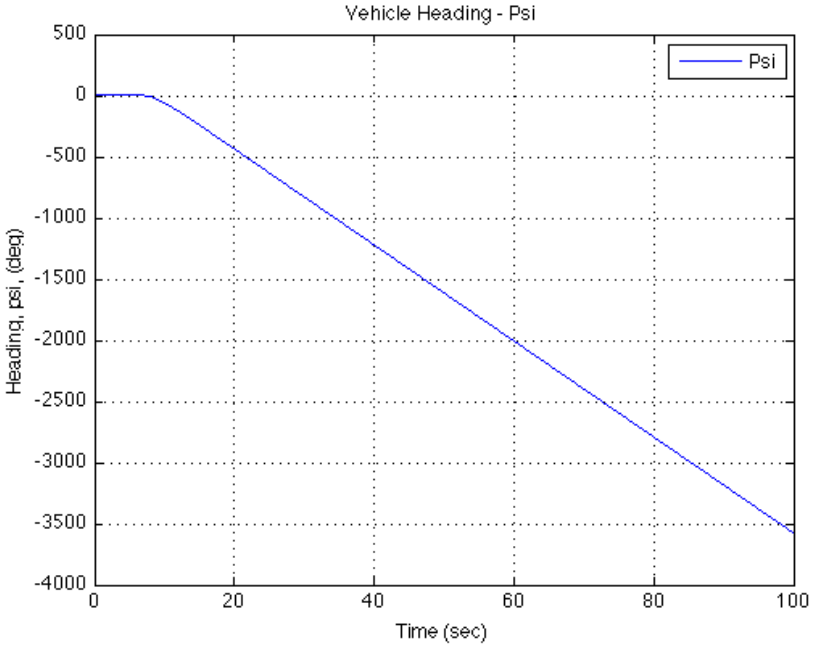

Figure 30. Heading Plot, PID Control Implemented

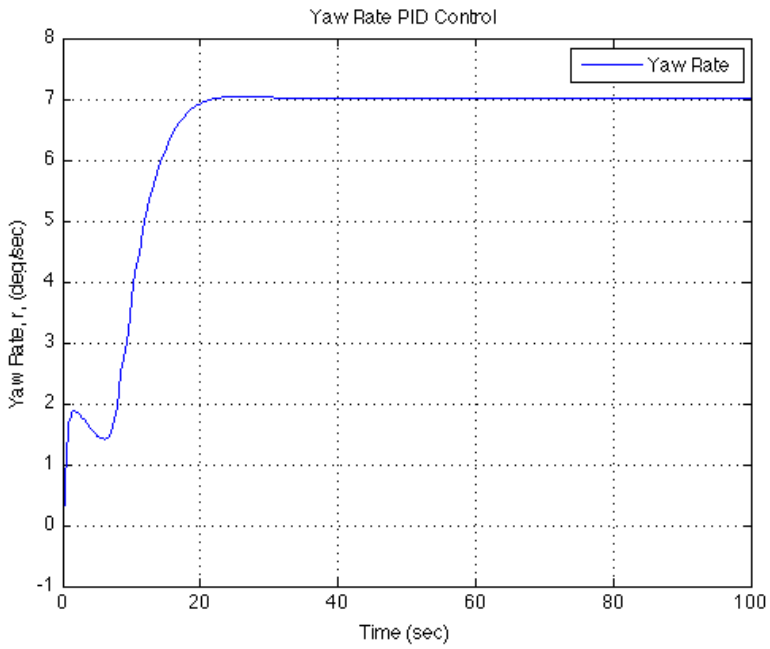

Figure 31. PID Control for Yaw Rate

As expected, the PID controller forces the yaw rate to converge to the commanded rate of $7\left[\frac{\text{deg}}{s}\right]$, resulting in the linear heading change shown in Figure 30. The positive buoyancy still results in the vehicle gradually surfacing, but the severe oscillatory behavior from inherent vehicle instabilities subsides.

C. MOTION CONTROL IN THE *X-Y* PLANE

Restricting vehicle control input to the forward and aft lateral cross-body thrusters only, motion control using a linearized model of the REMUS vehicle model in the horizontal plane is examined.

1. Model Linearization – Coupled Thruster Control

Using the following state vector:

$$\vec{x} = \begin{bmatrix} u & v & r & \psi \end{bmatrix}^T \tag{152}$$

assuming the forward and aft lateral thrusters are coupled:

$$n_{FLT} = -n_{SLT} = n \tag{153}$$

and eliminating non-linearity in the six degree-of-freedom model results in the following simplification of Equation (146):

$$\begin{bmatrix} (m - X_{\dot{u}}) & 0 & -my_{CG} & 0 \\ 0 & (m - Y_{\dot{v}}) & (mx_{CG} - Y_{\dot{r}}) & 0 \\ -my_{CG} & (mx_{CG} - N_{\dot{v}}) & (I_{zz} - N_{\dot{r}}) & 0 \\ 0 & 0 & 0 & 1 \end{bmatrix} \begin{bmatrix} \dot{u} \\ \dot{v} \\ \dot{r} \\ \dot{\psi} \end{bmatrix} =$$
$$\begin{bmatrix} X_{u|u|} & 0 & (X_{r|r|} - m) & 0 \\ 0 & Y_{v|v|} & (Y_{r|r|} - m) & 0 \\ 0 & N_{r|r|} & (N_{r|r|} - mx_{CG}) & 0 \\ 0 & 0 & 1 & 0 \end{bmatrix} \begin{bmatrix} u \\ v \\ r \\ \psi \end{bmatrix} + \begin{bmatrix} 0 \\ (F_{FLT} - F_{SLT}) \\ (M_{FLT} - M_{SLT}) \\ 0 \end{bmatrix} [n] \tag{154}$$

because the mass matrix remains invertible, Equation (154) can be expressed in the standard form of:

$$\dot{x} = [A]x + [B]u \tag{155}$$

where matrices *A* and *B* are used to determine controllability.

A system is completely controllable when the controllability matrix possesses full rank, where the controllability matrix is defined as:

$$Co = \begin{bmatrix} B & AB & A^2B & A^3B \end{bmatrix} \tag{156}$$

Substituting the appropriate coefficient values found in Appendix B yields the following matrices:

$$A = \begin{bmatrix} -0.0468 & 0 & -1.0490 & 0 \\ 0 & -1.9807 & -1.3368 & 0 \\ 0 & 0.0307 & -35.2346 & 0 \\ 0 & 0 & 1 & 0 \end{bmatrix}, \; B = \begin{bmatrix} 0 \\ 0.0399 \\ 0.0016 \\ 0 \end{bmatrix}$$
$$C = \begin{bmatrix} 0 & -0.0017 & 0.0582 & -2.0467 \\ 0.0399 & -0.0812 & 0.2350 & -3.0702 \\ 0.0016 & -0.0554 & 1.9486 & -68.6513 \\ 0 & 0.0016 & -0.0554 & 1.9486 \end{bmatrix} \tag{157}$$

where *n* was input as 2,000 RPM. The rank of the controllability matrix is four, and therefore full, indicating the system is controllable. Implementation of this controllable

linear model indicates that the vehicle can be controlled via commanded states, such as a desired heading, $\psi_{command}$, or desired location in the *x*-*y* plane.

2. Model Linearization – Thruster Differential Analysis

Validation of the non-linear model requires an analysis of the applied moment in both the horizontal and vertical planes of motion. This differential is then implemented into the REMUS vehicle itself for comparison to the computer model.

a. Lateral Thruster Differential

Due to non-symmetrical placement of the cross-body thrusters, an inherent moment exists when equal thruster RPM commands are input into the model. Using the linearized model, several simulations were run holding the forward thruster constant and varying stern lateral thruster speeds analyzing vehicle response to a commanded yaw rate of $5\left[\text{deg}/s\right]$. Table 10 presents the results:

FLT [RPM]	SLT [RPM]	Thruster Differential [RPM]
500	-300	200
1000	-700	300
1500	-1400	100
2000	-1900	100
2500	-2300	200
3000	-2600	400
3500	-3300	200
4000	-3600	400
4500	-4000	500
5000	-4500	500

Table 10. Lateral Cross-Body Thruster Differential

This results in an average thruster differential of 290 RPM. Figure 32 presents the implementation of this differential into the linear model with no PID control:

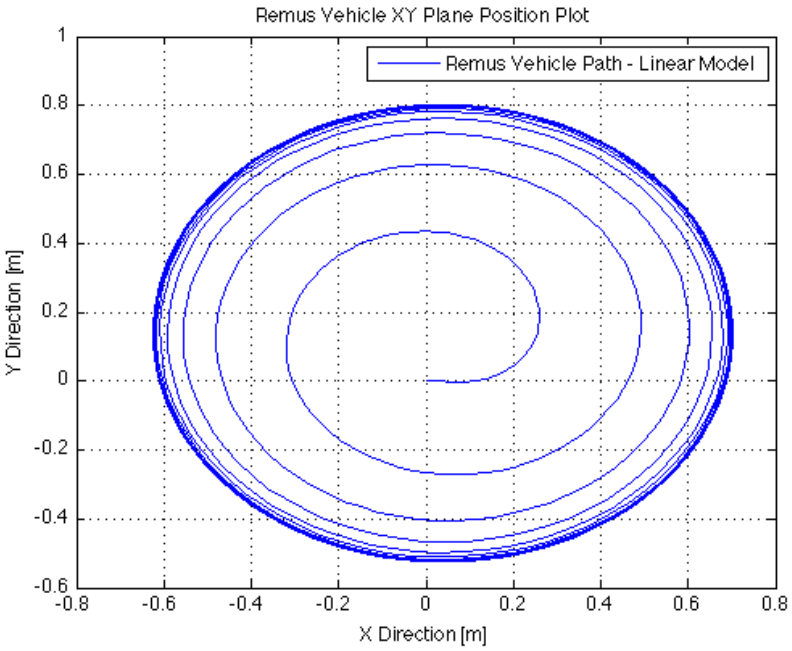

Figure 32. X-Y Plane, Linear Model

Applying the constant thruster differential to the model minimizes vehicle motions in the *x-y* plane.

b. Vertical Thruster Differential

The vertical thruster differential was determined using a similar analysis applied to the lateral thrusters. Once more, the forward vertical thruster was held constant and the stern vertical thruster was varied to achieve a commanded pitch of $0\left[\text{deg}\right]$. Table 11 presents the results:

FVT [RPM]	SVT [RPM]	Thruster Differential [RPM]
500	-200	300
1000	-550	450
1500	-1100	400
2000	-1550	450
2500	-2100	400
3000	-2550	450
3500	-2950	550
4000	-3400	600
4500	-4000	500
5000	-4450	550

Table 11. Vertical Cross-Body Thruster Differential

These simulations result in an average vertical thruster differential of 465 RPM. Figure 33 presents the implementation of the averaged thruster differential into the linear model with no PID control.

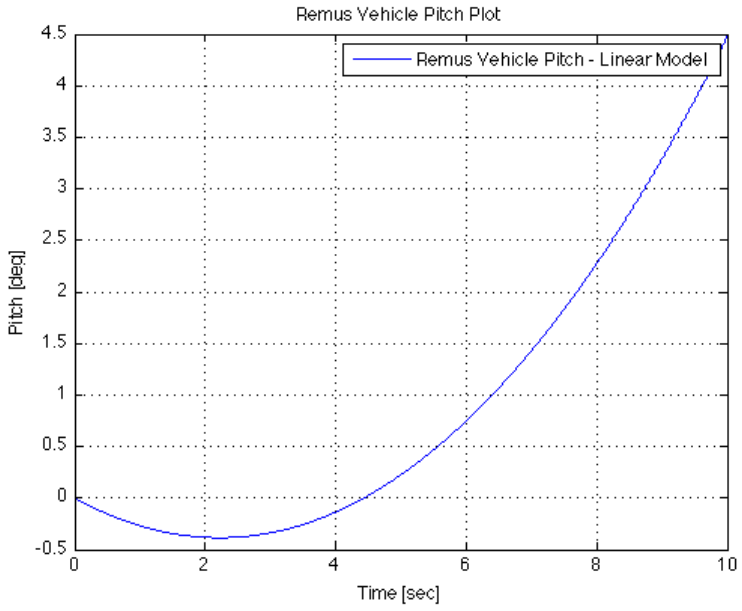

Figure 33. Vehicle Pitch, Linear Model

The thrust differential briefly forces the vehicle to small perturbations in pitch, but requires detailed controllability analysis and implementation of a controller to prevent the instability in the vehicle model from growing unbounded as in Figure 33.

VII. CONCLUSIONS

A. INTRODUCTION

This chapter presents an analysis of results, conclusions drawn and possible avenues of future study. Recall that non-linear vehicle model simulations utilized equivalent thruster control to force the vehicle to rotate about its center, minimizing vehicle movement in the horizontal plane, while the linear vehicle model analyzed the thruster induced moments on the vehicle.

B. ANALYSIS OF RESULTS

1. Hydrodynamic Coefficients

A significant amount of time was spent developing the required hydrodynamic coefficients for this latest version of the REMUS vehicle. These coefficients As stated previously, the coefficients remain dimensional for ease of comparison with the coefficients from the original REMUS vehicle [12]. Significant deviations in coefficient values occurred. A simple unit analysis for the non-linear force coefficients shows that the primary contributions to many of the coefficients are from mass $[kg]$ and a length $[m]$, either radial or axial. Given that the vehicle mass and axial length is significantly larger; their impact on respective coefficients is proportionately larger. Similarly, the non-linear moment coefficients generally possess units of mass $[kg]$ and area $[m^2]$, resulting in even larger deviations from values determined in [12].

2. Vehicle Modeling

Implementation of the derived hydrodynamic coefficients results in an accurate non-linear model of true REMUS vehicle motions. This is evident in the required thruster differential due to non-symmetrical placement of the cross-body thrusters. Simulations using the non-linear model with equal and opposite thruster inputs results in a sinusoidal path of advance caused by unequal moments generated by the thruster pairs. To minimize these motions in the horizontal plane, the stern lateral thruster requires a setting of 290 RPM less than the forward lateral thruster to eliminate the unequal

moment. Similarly, for the vertical thrusters, a differential of 465 RPM is required to minimize vehicle pitch while ascending or descending. However, a more thorough comparison between actual in-water data and simulation results needs to be conducted to fully validate this REMUS vehicle model. Tow tank experiments validating the radial and axial drag coefficients are of particular interest, since the significant size differential forces large differences between the derived hydrodynamic terms in this work and those in [12].

3. Vehicle Control

Implementation of a PID control for yaw rate through controllability analysis of a linear model further supports the validity of the REMUS vehicle model. Although only a single batch of simulation results is presented; the vehicle model tracks as commanded to any desired yaw rate within the model boundaries of $0\left[\text{deg}/s\right]$ to $14.5\left[\text{deg}/s\right]$. The yaw rate boundary limits are dependent upon the minimum and maximum thruster range of 0 RPM to 5,000 RPM. In depth thruster analysis remains to be executed to provide a fully controllable thruster model in closed loop control. Of particular interest is the contribution of individual thruster pairs to their respective angular velocities and accelerations, as well as the effects of slaved and non-slaved thruster pairs to the vehicle dynamics. Implementation of closed loop control requires this detailed analysis of the thrusters on the vehicle dynamics and would facilitate faster response time to track the desired yaw rate.

C. FUTURE WORK

The modularity of the REMUS vehicle provides a unique foundation for continuous work in the field of autonomous underwater vehicles. This work provides a logical origin for follow-on study, particularly in the following fields:

- *Object Avoidance* – Implementation of cross-body thruster control during object avoidance maneuvers can be analyzed and compared to results found in [13], enabling further study in the field of optimal control, generating logic algorithms optimizing thruster and control surface use to achieve a goal or series of goals.

- *Simultaneous Localization and Mapping (SLAM)* – The robust model reduces errors in state space estimates, thereby reducing the area of uncertainty in the localization process.
- *Model Reference Adaptive Control (MRAC)* – A valid vehicle model enables the implementation of MRAC to provide adjustable closed loop control of the REMUS vehicle.
- *Multiple AUV Operations* – A robust model of each vehicle in simultaneous operations allows more coordinated command and control by the designated lead vehicle to ensure reliable operation and mission completion.
- *AUV Operations in Larger Operating Envelopes* – A robust on-board model permits the AUV to operate outside the normal environmental tolerances. Feedback sensors combined with sea-state prediction algorithms would expand AUV use to encompass a wider array of military and civilian operating environments.

THIS PAGE INTENTIONALLY LEFT BLANK

APPENDIX A. TABLES OF PARAMETERS

A.1 STANDARD REMUS HULL PARAMETERS

Parameter	Value	Units	Description
ρ	1.03e+03	$\left[kg/m^3\right]$	Seawater Density
L	2.72415e+00	$[m]$	Vehicle Length
D	1.9e-01	$[m]$	Vehicle Maximum Diameter
m	6.60399e+1	$[kg]$	Vehicle Mass
W	6.4785e+2	$[N]$	Vehicle Weight
B	6.9799e+2	$[N]$	Vehicle Buoyancy
A_f	2.84e-2	$[m^2]$	Hull frontal area
A_p	4.786e-1	$[m^2]$	Hull projected area (x-z plane)

Table 12. REMUS Hull Parameters

A.2 CENTER OF BUOYANCY RELATIVE TO ORIGIN AT VEHICLE NOSE

Parameter	Value	Units	Description
x_{CB}	-1.362075e0	$[m]$	Longitudinal Center of Buoyancy
y_{CB}	0.00	$[m]$	Transverse Center of Buoyancy
z_{CB}	0.00	$[m]$	Vertical Center of Buoyancy

Table 13. Center of Buoyancy

A.3 CENTER OF GRAVITY RELATIVE TO ORIGIN AT VEHICLE HALF LENGTH

Parameter	Value	Units	Description
x_{CG}	1.4325e-2	$[m]$	Longitudinal Center of Gravity
y_{CG}	0.00	$[m]$	Transverse Center of Gravity
z_{CG}	-4.7625e-2	$[m]$	Vertical Center of Gravity

Table 14. Center of Gravity

A.4 HULL COORDINATES FOR LIMITS OF INTEGRATION RELATIVE TO ORIGIN AT VEHICLE HALF LENGTH

Following the notation used in [12].

Parameter	Value	Units	Description
x_t	-1.362075e0	$[m]$	Aft End of Tail Section
x_{t_2}	-6.40975e-1	$[m]$	Forward End of Tail Section
x_f	-1.235075e0	$[m]$	Aft End of Fin Section
x_{f_2}	-1.150975e0	$[m]$	Forward End of Fin section
x_b	8.35025e-1	$[m]$	Aft End of Bow Section
x_{b_2}	1.360275e0	$[m]$	Forward End of Bow Section

Table 15. Hull Coordinates for Limits of Integration

A.5 STANDARD REMUS FIN PARAMETERS

Parameter	Value	Units	Description
s_{fin}	6.65e-03	$\left[m^2 \right]$	Plan form area
b_{fin}	8.57e-02	$[m]$	Fin Span
a_{fin}	1.39e-01	$[m]$	Maximum Fin Height above centerline
a_{avg}	1.17e-01	$[m]$	Average Fin Height above centerline
c_{df}	5.58e-01		Cross-flow drag coefficient
t	5.31e-01		Fin Taper Ratio
x_{fin}	-6.85e-01	$[m]$	Fin post location relative to origin at $\frac{l}{2}$

Table 16. Standard REMUS Fin Parameters

THIS PAGE INTENTIONALLY LEFT BLANK

APPENDIX B. TABLES OF COMBINED NON-LINEAR COEFFICIENTS

B.1 NON-LINEAR FORCE COEFFICIENTS

Parameter	Value	Units	Description
X_{uu}	-3.13e0	$\left[kg/m \right]$	Axial Drag coefficient in surge
$X_{\dot{u}}$	-8.84e-1	$[kg]$	Axial Added Mass coefficient in surge
X_{wq}	-7.78e+1	$\left[kg/rad \right]$	Surge cross-term in heave and pitch
X_{qq}	-4.16e0	$\left[kg \cdot m/rad \right]$	Surge drag coefficient in pitch
X_{vr}	7.78e+1	$\left[kg/rad \right]$	Surge cross-term in sway and yaw
X_{rr}	-4.16e0	$\left[kg \cdot m/rad \right]$	Surge drag coefficient in yaw
Y_{vv}	-2.85e+2	$\left[kg/m \right]$	Axial drag coefficient in sway
Y_{rr}	1.30e+1	$\left[kg \cdot m/rad^2 \right]$	Sway coefficient in yaw
Y_{uv}	1.16e+1	$\left[kg/m \right]$	Body lift force and fin lift
$Y_{\dot{v}}$	-7.78e+1	$[kg]$	Axial Added Mass coefficient in sway
$Y_{\dot{r}}$	4.16e0	$\left[kg \cdot m/rad \right]$	Added mass coefficient in yaw
Y_{ur}	-8.84e-1	$\left[kg/rad \right]$	Sway cross-term in surge and yaw
Y_{wp}	7.78e+1	$\left[kg/rad \right]$	Sway cross-term in heave and roll
Y_{pq}	4.16e0	$\left[kg \cdot m/rad \right]$	Sway cross-term in roll and pitch
$Y_{uu\delta_r}$	2.13e+1	$\left[kg \cdot m/rad \right]$	Fin lift force coefficient (rudder)

Z_{ww}	-2.85e+2	$\left[kg/m \right]$	Axial drag coefficient in heave
Z_{qq}	1.30e+1	$\left[kg \cdot m/rad^2 \right]$	Heave coefficient in pitch
Z_{uw}	1.16e+1	$\left[kg/m \right]$	Body lift force and fin lift
$Z_{\dot{w}}$	-7.78e+1	$[kg]$	Axial Added Mass coefficient in heave
$Z_{\dot{q}}$	-4.16e+0	$\left[kg \cdot m/rad \right]$	Added mass in pitch
Z_{uq}	8.84e-1	$\left[kg/rad \right]$	Heave cross-term in surge and pitch
Z_{vp}	-7.78e+1	$\left[kg/rad \right]$	Heave cross-term in sway and roll
Z_{rp}	4.16e0	$\left[kg/rad \right]$	Heave cross-term in roll and yaw
$Z_{uu\delta_s}$	-2.13e+1	$\left[kg/m \cdot rad \right]$	Fin lift force coefficient (stern-plane)

Table 17. Non-Linear Force Coefficients

B.2 NON-LINEAR MOMENT COEFFICIENTS

Parameter	Value	Units	Description
K_{pp}	-1.30e-1	$\left[kg \cdot m^2/rad^2 \right]$	Axial rolling drag
$K_{\dot{p}}$	-1.04e-2	$\left[kg \cdot m^2/rad^2 \right]$	Added mass moment in roll
M_{ww}	-8.82e0	$[kg]$	Cross-flow drag in heave
M_{qq}	-2.81e+3	$\left[kg \cdot m^2/rad^2 \right]$	Cross-flow drag in pitch
M_{uw}	-5.48e-1	$[kg]$	Body lift and fin lift
$M_{\dot{w}}$	-4.16e0	$[kg \cdot m]$	Added mass moment in heave
$M_{\dot{q}}$	-4.52e+1	$\left[kg \cdot m^2/rad \right]$	Added mass moment in pitch
M_{uq}	4.16e0	$\left[kg \cdot m/rad \right]$	Added mass moment cross-term

			in surge and pitch
M_{vp}	-4.16e0	$\left[kg \cdot m / rad \right]$	Added mass moment cross-term in sway and roll
M_{rp}	4.52e+1	$\left[kg \cdot m^2 / rad^2 \right]$	Added mass moment cross-term in roll and pitch
$M_{uu\delta_r}$	-1.46e+1	$\left[kg / rad \right]$	Fin lift moment (rudder)
N_{vv}	8.82e0	$[kg]$	Cross-flow drag in sway
N_{rr}	-2.81e+3	$\left[kg \cdot m^2 / rad^2 \right]$	Cross-flow drag in yaw
N_{uv}	5.48e-1	$[kg]$	Body lift and fin lift
$N_{\dot{v}}$	4.16e0	$[kg \cdot m]$	Added mass moment in sway
$N_{\dot{r}}$	-4.52e+1	$\left[kg \cdot m^2 / rad \right]$	Axial added mass moment in yaw
N_{ur}	4.16e0	$\left[kg \cdot m / rad \right]$	Added mass moment cross-term in surge and yaw
N_{wp}	-4.16e0	$\left[kg \cdot m / rad \right]$	Added mass moment cross-term in heave and roll
N_{pq}	-4.52e+1	$\left[kg \cdot m^2 / rad^2 \right]$	Added mass moment cross-term in roll and pitch
$N_{uu\delta_s}$	-1.46e+1	$\left[kg / rad \right]$	Fin lift moment (stern-plane)

Table 18. Non-Linear Moment Coefficients

THIS PAGE INTENTIONALLY LEFT BLANK

APPENDIX C. MATLAB CODE

C.1 EMBEDDED MATLAB FUNCTION: REMUS.M

```
function [x_dot,p_dot, a_dot, F, F_prop, U] = remus(x,ui)
%% Author: Sean Doherty
%% Date: 30 September 2010
%% Revision: 17th
%% Revision Date: 27 February 2011
%% References :
%       L. R. Fodrea, "Obstacle Avoidance Control for the REMUS Autonomous
%          Underwater Vehicle." M.S. Thesis, Naval Postgraduate School,
%          Monterey, California, USA, 2002. [Print].
%
%       T. I. Fossen and T. Perez, _Marine Systems Simulator (MSS),_
%          developed at the Norwegian University of Science and
%          Technology, 2010. [Online] Software Available:
%          http://www.marinecontrol.org/. [Accessed: 5 March 2010].
%
%       T. Prestero, "Verification of a Six-Degree of Freedom Simulation
%          Model for the REMUS Underwater Vehicle." M.S. Thesis,
%          Massachusetts Institute of Technology, Cambridge,
%          Massachusetts, USA, 2001. [Print].
%
%% Details:
%
% [xdot,F,U, F_prop] = remus(x,ui) gives the derivative of the state vector:
% x = [ u v w p q r x y z phi theta psi ]' for the REMUS AUV. All
% requisite parameters and hydrodynamic coefficients are  included within
% this function.
%_____________________________________________________________________
% Inputs:
% The state vector is defined as:
%
% x     = [u v w p q r xpos ypos zpos phi theta psi]' where
%
% u     = surge velocity         (m/s)
% v     = sway velocity          (m/s)
% w     = heave velocity         (m/s)
% p     = roll velocity          (rad/s)
% q     = pitch velocity         (rad/s)
% r     = yaw velocity           (rad/s)
% xpos  = position in x-direction (m)
% ypos  = position in y-direction (m)
```

```
% zpos  = position in z-direction (m)
% phi   = roll angle             (rad)
% theta = pitch angle            (rad)
% psi   = yaw angle              (rad)
%
% The input vector is :
%
% ui      = [ delta_r delta_p flt slt fvt svt n ]'  where
%
% delta_r  = rudder angle                 (deg)
% delta_p  = port and starboard stern plane (deg)
% flt      = forward lateral thruster      (RPM)
% slt      = stern lateral thruster        (RPM)
% fvt      = forward vertical thruster     (RPM)
% svt      = stern vertical thruster       (RPM)
% n        = main propeller shaft speed    (percent max thrust)
%
%_____________________________________________________________________
% Outputs:
%
% Speed:           U      = (m/s)
% Forces:          F      = [X Y Z K M N]'
%                  F_prop = [X_prop Y_prop Z_prop K_prop M_prop N_prop]'
% Accelerations:   xdot   = [Xdot Ydot Zdot Kdot Mdot Ndot]'
%
%_____________________________________________________________________
%% Note:
% Portions of this code were adapted from the MSS GNC toolkit.
% The MSS GNC is a Matlab toolbox for guidance, navigation and control.
% The toolbox is part of the Marine Systems Simulator (MSS).
%
% Copyright (C) 2008 Thor I. Fossen and Tristan Perez
%
% This program is free software: you can redistribute it and/or modify
% it under the terms of the GNU General Public License as published by
% the Free Software Foundation, either version 3 of the License, or
% (at your option) any later version.
%
% This program is distributed in the hope that it will be useful, but
% WITHOUT ANY WARRANTY; without even the implied warranty of
% MERCHANTABILITY or FITNESS FOR A PARTICULAR PURPOSE.  See the
% GNU General Public License for more details.
%
% You should have received a copy of the GNU General Public License
% along with this program.  If not, see <http://www.gnu.org/licenses/>.
```

```
%
% E-mail: contact@marinecontrol.org
% URL:    <http://www.marinecontrol.org>
%_____________________________________________________________________
%% Verification of input and state dimensions
if (length(x) ~= 12),error('x-vector must have dimension 12 !');end
if (length(ui) ~= 7),error('u-vector must have dimension 7 !');end

%% Dimensional states
u   = x(1);  v     = x(2);  w   = x(3);
p   = x(4);  q     = x(5);  r   = x(6);
phi = x(10); theta = x(11); psi = x(12);

U = sqrt(u^2+v^2+w^2); % speed

% Reorganizing dimensional states:

%nu = [u v w p q r]';

%% REMUS Vehicle Measurements (taken 28 October 2010):
%L = 2.72415;     % Length in meters (m) [includes BlueView Package]
%D = 0.19;        % Maximum diameter in meters (m)
g = 9.81;         % Acceleration due to gravity in meters/second^2 (m/s^2)
m = 66.0399;      % Mass in kilgrams (kg)
W = m*g;          % Weight in Newtons (N)
B = (m+0.5)*g;    % Measured Vehicle Buoyancy (N)
V_max = 2.881;    % Maximum Forward Velocity (m/s)

%   Moments of Inertia WRT Origin at Half-Length
I_xx = 1.154E0;        % kg*m^2
I_yy = 3.470E1;        % kg*m^2
I_zz = I_yy;           % kg*m^2
I_yz = 5.768E-1;
I_zy = I_yz;

%   Center of Buoyancy WRT Origin at Vehicle Nose
x_cb = -1.36208E0;       % x-location (m)
y_cb = 0.00;             % y-location (m)
z_cb = 0.00;             % z-location (m)

%   Center of Gravity WRT Origin at Vehicle Nose
x_cg = 1.4325E-2;        % x-location (m)
y_cg = 0.00;             % y-location (m)
z_cg = -1.016E-1;        % z-location (m)
```

```
%   Non-Linear Force Coefficients

X_uu   = -3.13E0;        % Cross-flow Drag (kg/m)
X_udot = -8.84E-1;       % Added Mass (kg)
X_wq   = -7.78E1;        % Added Mass Cross-term (kg/rad)
X_qq   = -4.16E0;        % Added Mass Cross-term (kg*m/rad)
X_vr   =  7.78E1;        % Added Mass Cross-term (kg/rad)
X_rr   = -4.16E0;        % Added Mass Cross-term (kg*m/rad)

Y_vv   = -2.85E2;        % Cross-flow Drag (kg/m)
Y_rr   = -1.30E1;        % Cross-flow Drag (kg*m/rad^2)
Y_uv   =  1.16E1;        % Body Lift Force and Fin Lift (kg/m)
Y_vdot = -X_vr;          % Added Mass (kg)
Y_rdot = -X_rr;          % Added Mass (kg*m/rad)
Y_ur   =  X_udot;        % Added Mass Cross-term and Fin Lift (kg/rad)
Y_wp   = -X_wq;          % Added Mass Cross-term (kg/rad)
Y_pq   = -X_qq;          % Added Mass Cross-term (kg*m/rad)
Y_uudr =  2.13E1;        % Fin Lift Force (kg/(m*rad))

Z_ww   =  Y_vv;          % Cross-flow Drag (kg/m)
Z_qq   = -Y_rr;          % Cross-flow Drag (kg*m/rad)
Z_uw   =  Y_uv;          % Body Lift Force and Fin Lift (kg/m)
Z_wdot =  X_wq;          % Added Mass (kg)
Z_qdot =  X_qq;          % Added Mass (kg*m/rad)
Z_uq   = -X_udot;        % Added Mass Cross-term and Fin Lift (kg/rad)
Z_vp   =  Y_vdot;        % Added Mass Cross-term (kg/rad)
Z_rp   =  Y_rdot;        % Added Mass Cross-term (kg/rad)
Z_uuds = -2.13E1;        % Fin Lift Force (kg/(m*rad))

%   Non-Linear Moment Coefficients

K_pp   = -1.30E-1;       % Rolling Resistance (kg*m^2/rad^2)
K_pdot = -1.04E-2;       % Added Mass (kg*m^2/rad)

M_ww   = -8.82E0;        % Cross-flow Drag (kg)
M_qq   = -2.81E3;        % Cross-flow Drag (kg*m^2/rad^2)
M_uw   = -5.48E-1;       % Body and Fin Lift and Munk Moment (kg)
M_wdot =  Z_qdot;        % Added Mass (kg*m)
M_qdot = -4.52E1;        % Added Mass (kg*m^2/rad)
M_uq   = -X_qq;          % Added Mass Cross-term and Fin Lift (kg*m/rad)
M_vp   = -M_uq;          % Added Mass Cross-term (kg*m/rad)
M_rp   =  4.52E1;        % Added Mass Cross-term (kg*m^2/rad^2)
M_uuds = -1.46E1;        % Fin Lift Moment (kg/rad)

N_vv   = -M_ww;          % Cross-flow Drag (kg)
```

```
N_rr   =  M_qq;          % Cross-flow Drag (kg*m^2/rad^2)
N_uv   =  5.48E-1;       % Body and Fin Lift and Munk Moment (kg)
N_vdot =  Y_rdot;        % Added Mass (kg*m)
N_rdot =  M_qdot;        % Added Mass (kg*m^2/rad)
N_ur   =  M_uq;          % Added Mass Cross-term and Fin Lift (kg*m/rad)
N_wp   = -N_ur;          % Added Mass Cross-term (kg*m/rad)
N_pq   = -M_rp;          % Added Mass Cross-term (kg*m^2/rad^2)
N_uudr =  M_uuds;        % Fin Lift Moment (kg/rad)

%   Rigid Body Mass Matrix:

M11 = [m 0 0;
       0 m 0;
       0 0 m];

M12 = [    0      (m*z_cg)      (-m*y_cg);
       (-m*z_cg)      0         (m*x_cg);
        (m*y_cg) (-m*x_cg)          0  ];

M21 = [    0      (-m*z_cg)      (m*y_cg);
       (m*z_cg)      0         (-m*x_cg);
      (-m*y_cg)   (m*x_cg)          0  ];

M22 = [I_xx    0       0;
       0    I_yy    -I_yz;
       0   -I_zy     I_zz];

%  Added Mass Matrix:
MA11 = [X_udot    0     0;
        0    Y_vdot   0;
        0       0   Z_wdot];

MA12 = [  0       0     0;
          0       0   Y_rdot;
          0    Z_qdot   0];

MA21 = [  0       0     0;
          0       0   M_wdot;
          0    N_vdot   0];

MA22 = [K_pdot    0     0;
          0    M_qdot   0;
          0       0   N_rdot];

%   Total Mass Matrix (M-MA):
```

```
MM = [(M11-MA11)  (M12-MA12);
     (M21-MA21)  (M22-MA22)];

InvM = inv(MM);

%%

c1 = cos(phi);
c2 = cos(theta);
c3 = cos(psi);
s1 = sin(phi);
s2 = sin(theta);
s3 = sin(psi);
t2 = tan(theta);

%% Control input (rudder, plane, thrusters and propeller)
delta_r  = ui(1);               % Angle   (rad)
delta_p  = ui(2);               % Angle   (rad)

%   Thruster Terms (Cross-body thruster data taken 1 November 2010)

%       Main Thruster (from Prestero Thesis):
n_max  =  X_uu*V_max*abs(V_max);     % Propeller Max Thrust (N)
n_maxT = (0.995*((W*y_cg)-(B*y_cb)))-(0.093*((W*z_cg)-(B*z_cb))); % Propeller
Max Torque (N*m)
n      = ((ui(7)/100)*n_max);       % Thrust  (N)
n_t    = ((ui(7)/100)*n_maxT);      % Torque (N-m)

%       Cross-body Thruster Thrust (N):

flt      = (-4E-14*ui(3)^4)+(3E-10*ui(3)^3)-(2E-7*ui(3)^2)+...
           (0.0004*ui(3))-0.0054;
slt      = (-4E-14*ui(4)^4)+(3E-10*ui(4)^3)-(2E-7*ui(4)^2)+...
           (0.0004*ui(4))-0.0054;
fvt      = (-4E-14*ui(5)^4)+(3E-10*ui(5)^3)-(2E-7*ui(5)^2)+...
           (0.0004*ui(5))-0.0054;
svt      = (-4E-14*ui(6)^4)+(3E-10*ui(6)^3)-(2E-7*ui(6)^2)+...
           (0.0004*ui(6))-0.0054;

%       Cross-Body Thruster Torque (N-m):

flt_t    = (-4.702E-14*ui(3)^4)+(3.302E-10*ui(3)^3)-(2.700E-7*ui(3)^2)+...
           (4.360E-4*ui(3))-(6.290E-3);
slt_t    = (1.653E-14*ui(4)^4)-(1.161E-10*ui(4)^3)+(9.489E-8*ui(4)^2)-...
```

```
        (1.532E-4*ui(4))+(2.211E-3);
fvt_t   = (-4.523E-14*ui(5)^4)+(3.176E-10*ui(5)^3)-(2.597E-7*ui(5)^2)+...
        (4.193E-4*ui(5))-(6.050E-3);
svt_t   = (1.832E-14*ui(6)^4)-(1.287E-10*ui(6)^3)+(1.052E-7*ui(6)^2)-...
        (1.699E-4*ui(6))+(2.451E-3);

%% Cross-body Thruster Forces and Moments:

X_prop = n;
Y_prop = flt + slt;
Z_prop = fvt + svt;
K_prop = n_t;
M_prop = flt_t + slt_t;
N_prop = fvt_t + svt_t;

F_prop = [X_prop Y_prop Z_prop K_prop M_prop N_prop]';

%% Total Forces and Moments from Equations of Motion
%   Equations of Motion obtained from the Prestero thesis.  Specifically,
%   equations (3.8) and (4.49) are used.  The initial time derivatives of
%   the state vector are assumed to be zero

%   Surge Equation of Motion:
X = -((W-B)*sin(theta)) + (X_uu*u*abs(u)) + ((X_wq-m)*w*q) + ...
   ((X_qq-(m*x_cg))*q^2) + ((X_vr+m)*v*r) + ((X_rr+(m*x_cg))*r^2) - ...
   (m*y_cg*p*q) - (m*z_cg*p*r) + X_prop;

%   Sway Equation of Motion:
Y = ((W-B)*cos(theta)*sin(phi)) + (Y_vv*v*abs(v)) + (Y_rr*r*abs(r)) + ...
   (m*y_cg*r^2) + ((Y_ur-m)*u*r) + ((Y_wp-m)*w*p) + ...
   ((Y_pq-(m*x_cg))*p*q) + (Y_uv*u*v) + (m*y_cg*p^2) + ...
   ((m*z_cg)*q*r) + (Y_uudr*u^2*delta_r) + Y_prop;

%   Heave Equation of Motion:
Z = ((W-B)*cos(theta)*cos(phi)) + (Z_ww*w*abs(w)) + (Z_qq*q*abs(q)) + ...
   ((Z_uq+m)*u*q) + ((Z_vp-m)*v*p) + ((Z_rp-(m*x_cg))*r*p) + ...
   (Z_uw*u*w) + ((m*z_cg)*(p^2+q^2)) - (m*y_cg*r*q) + ...
   (Z_uuds*u^2*delta_p) + Z_prop;

%   Roll Equation of Motion:
K = -(((y_cg*W)-(y_cb*B))*cos(theta)*cos(phi)) - ...
   (((z_cg*W)-(z_cb*B))*cos(theta)*sin(phi)) + (K_pp*p*abs(p)) - ...
   ((I_zz-I_yy)*q*r) - (I_yz*(r^2-q^2)) + (m*y_cg*((u*q)-(v*p))) - ...
   ((m*z_cg)*((w*p)-(u*r))) + K_prop;
```

```
%   Pitch Equation of Motion:
M = -(((z_cg*W)-(z_cb*B))*sin(theta)) - ...
    (((x_cg*W)-(x_cb*B))*cos(theta)*cos(phi)) + (M_ww*w*abs(w)) + ...
    (M_qq*q*abs(q)) + ((M_uq-(m*x_cg))*u*q) + ((M_vp-(m*x_cg))*v*p) + ...
    ((M_rp-(I_xx-I_zz))*r*p) - (I_yz*q*p) + ((m*z_cg)*((v*r)-(w*q))) + ...
    (M_uw*u*w) + (M_uuds*u^2*delta_p) + M_prop;

%   Yaw Equation of Motion:
N = -(((x_cg*W)-(x_cb*B))*cos(theta)*sin(phi)) + ...
    (((y_cg*W)-(y_cb*B))*sin(theta)) + (N_vv*v*abs(v)) + ...
    (N_rr*r*abs(r)) + ((N_ur-(m*x_cg))*u*r) + ((N_wp+(m*x_cg))*w*p) + ...
    ((N_pq-(I_yy-I_zz))*p*q) + (I_yz*r*p) - (m*y_cg*((v*r)-(w*q))) + ...
    (N_uv*u*v) + (N_uudr*u^2*delta_r) + N_prop;

F = [X Y Z K M N]';

%% Accelerations:
x_dot = ...
 [InvM(1,1)*X+InvM(1,2)*Y+InvM(1,3)*Z+InvM(1,4)*K+InvM(1,5)*M+InvM(1,6)*N;
  InvM(2,1)*X+InvM(2,2)*Y+InvM(2,3)*Z+InvM(2,4)*K+InvM(2,5)*M+InvM(2,6)*N;
  InvM(3,1)*X+InvM(3,2)*Y+InvM(3,3)*Z+InvM(3,4)*K+InvM(3,5)*M+InvM(3,6)*N;
  InvM(4,1)*X+InvM(4,2)*Y+InvM(4,3)*Z+InvM(4,4)*K+InvM(4,5)*M+InvM(4,6)*N;
  InvM(5,1)*X+InvM(5,2)*Y+InvM(5,3)*Z+InvM(5,4)*K+InvM(5,5)*M+InvM(5,6)*N;
 InvM(6,1)*X+InvM(6,2)*Y+InvM(6,3)*Z+InvM(6,4)*K+InvM(6,5)*M+InvM(6,6)*N];

p_dot = ...
   [(c3*c2*u) + (((c3*s2*s1)-(s3*c1))*v) + (((s3*s1)+(c3*c1*s2))*w);
    (s3*c2*u) + (((c1*c3)+(s1*s2*s3))*v) + (((c1*s2*s3)-(c3*s1))*w);
      (-s2*u) +             (c2*s1*v) +             (c1*c2*w)];

a_dot = ...
        [(p) +             (s1*t2*q) +             (c1*t2*r);
                           (c1*q) -                (s1*r);
                      ((s1/c2)*q) +           ((c1/c2)*r)];
```

C.2 REMUS VEHICLE MODEL BLOCK DIAGRAM

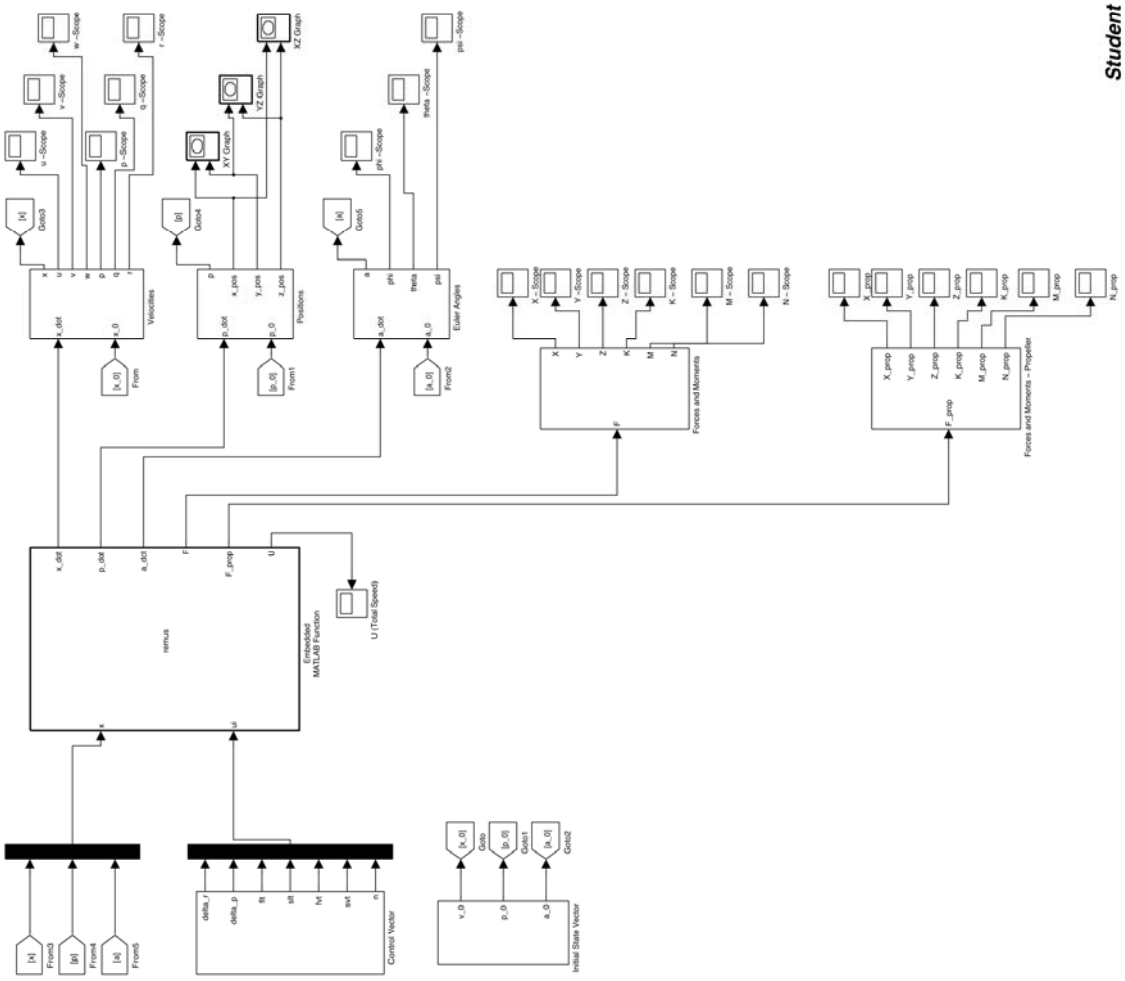

THIS PAGE INTENTIONALLY LEFT BLANK

LIST OF REFERENCES

[1] Museo Galileo, "Leonardo da Vinci – Studies on Keels of Unsinkable Ships," Museo Galileo Institute and Museum of the History of Science, 2010. [Online] Available: http://brunelleschi.imss.fi.it/genscheda.asp?appl=LIR&xsl=paginamanoscritto&lingua=ENG&chiave=101406. [Accessed: 10 October 2010].

[2] Museo Galileo, "Leonardo da Vinci – Machine for Raising Water, Diver and Equipment to Allow People to Walk on Water," Museo Galileo Institute and Museum of the History of Science, 2010. [Online] Available: http://brunelleschi.imss.fi.it/genscheda.asp?appl=LIR&xsl=paginamanoscritto&lingua=ENG&chiave=101365. [Accessed: 10 October 2010].

[3] G. Antonelli, *Underwater Robots: motion and Force Control of Vehicle Manipulator Systems*, 2nd ed., B. Siciliano, O. Khatib, and F. Groen, Ed. Berlin, Germany: Springer, 2006. [Print].

[4] G. Pararas-Carayannis, "Turtle: A Revolutionary Submarine," *Sea Frontiers*, Vol. 22 No. 4, pp. 234, July–August 1976. [Online] Excerpts Available: http://www.drgeorgepc.com/Turtle.html. [Accessed: 11 October 2010].

[5] D. Blidberg, "The Development of Autonomous Underwater Vehicles (AUV): A Brief Summary," presented at IEEE International Conference on Robotics and Automation 2001, ICRA 2001, Seoul, South Korea, 21-26 May 2001. [Online] Available: http://ausi.org/publications/ICRA_01paper.pdf. [Accessed: 23 September 2010].

[6] Woods Hole Oceanographic Institution (WHOI), "Ships and Vehicles Used in 1985 Discovery of *Titanic*," 1 March 2004, [Online] Available: http://www.whoi.edu/page.do?pid=7542. [Accessed: 3 October 2010].

[7] Canadian Broadcasting Corporation (CBC News), "Robot Subs Trying to Stop Gulf Oil Leak," 25 April 2010, [Online] Available: http://www.cbc.ca/news/world/story/2010/04/25/oil-rig-leak.html. [Accessed: 3 October 2010].

[8] Commander, Naval Sea Systems Command, "U.S. Navy Diving Manual," U.S. Government Printing Office, Washington, D.C., USA, SS521-AG-PRO-010 Revision 6, 15 April 2008. [Online] Available: http://www.supsalv.org/00c3_publications.asp. [Accessed: 23 February 2011].

[9] Naval Postgraduate School, “AUV Phoenix,” Naval Postgraduate School Center for Autonomous Vehicle Research (CAVR), 2010. [Online] Available: http://www.nps.edu/Academics/Centers/CAVR/Vehicles/Phoenix.html. [Accessed: 5 February 2011].

[10] Naval Postgraduate School, “AUV ARIES,” Naval Postgraduate School Center for Autonomous Vehicle Research (CAVR), 2010. [Online] Available: http://www.nps.edu/Academics/Centers/CAVR/Vehicles/ARIES.html. [Accessed: 5 February 2011].

[11] Massachusetts Institute of Technology, “Odyssey IV Class,” Massachusetts Institute of Technology Sea Grant AUV Laboratory, 2010. [Online] Available: http://seagrant.mit.edu/media/publications/MITSG_10-5.pdf. [Accessed: 5 February 2011].

[12] T. Prestero, "Verification of a Six-Degree of Freedom Simulation Model for the REMUS Underwater Vehicle." M.S. Thesis, Massachusetts Institute of Technology, Cambridge, Massachusetts, USA, 2001. [Print]

[13] L. Fodrea, "Obstacle Avoidance Control for the REMUS Autonomous Underwater Vehicle." M.S. Thesis, Naval Postgraduate School, Monterey, California, USA, 2002. [Print].

[14] J. Reidel, "Seaway Learning and Motion Compensation in Shallow Waters for Small AUVs." Ph.D. Dissertation, Naval Postgraduate School, Monterey, California, USA, June 1999. [Print]

[15] L. Cooney, "Dynamic Response and Maneuvering Strategies of a Hybrid Autonomous Underwater Vehicle in Hovering." M.S. Thesis, Massachusetts Institute of Technology, Cambridge, Massachusetts, USA, 2009. [Print]

[16] C. von Alt, B. Allen, T. Austin, and R. Stokey, “Remote Environmental Measuring Units,” in *Proceedings of the 1994 Symposium on Autonomous Underwater Vehicle Techonology*, 19–20 July 1994, pp. 13–19.

[17] E. Creed, S. Glenn, O. Schofield, H. Barrier, R. Petrecca and J. Dobarro, “LEO-15 Observatory – The Next Generation,” in *Proceedings of the 2005 MTS/IEEE OCEANS Conference*, 26 June 2006, pp. 1–5.

[18] Hydroid, “REMUS 100 – The World’s Most Proven AUV,” Hydroid Inc, 2010. [Online] Available: http://www.hydroidinc.com/remus100.html. [Accessed: 28 February 2010].

[19] The Society of Naval Architects and Marine Engineer (SNAME), "Nomenclature for Treating the Motion of a Submerged Body Through a Fluid," The Society of Naval Architects and Marine Engineers, New York City, New York, USA, Technical and Research Bulletin No. 1-5, 1950. [Online] Available: http://www.itk.ntnu.no/fag/gnc/papers/Sname%201950.PDF. [Accessed: 27 February 2011].

[20] T. Fossen, *Guidance and Control of Ocean Vehicles.* New York: John Wiley and Sons, 1994. [Print]

[21] R. Blevins, *Formulas for Natural Frequency and Mode Shape*, Malabar, Florida, USA: Robert E. Krieger Publishing Company, 1979. [Print]

[22] H. Saunders, *Hydrodynamics in Ship Design Volume* 2, 2nd ed., New York City, New York, USA: The Society of Naval Architects and Marine Engineers, 1972. [Print]

[23] S. Hoerner, *Fluid Dynamic Drag*, Midland Park, New Jersey, USA: Published by the Author, 1965. [Print]

[24] L. Whicker and L. Felner, "Free-Stream Characteristics of a Family of Low Aspect-Ratio, All-Movable Control Surfaces for Application to Ship Design," Technical Report 933, David Taylor Model Basin, Washington, D.C., USA, 1958. [Print]

[25] E. Lewis, Ed., *Principles of Naval Architecture Volume 3: Motions in Waves and Controllability*, 2nd ed., Jersey City, New Jersey, USA: The Society of Naval Architects and Marine Engineers, 1988. [Print]

[26] M. Nahon, "A Simplified Dynamics Model for Autonomous Underwater Vehicles," in *Proceedings of the 1996 Symposium on Autonomous Underwater Vehicle Technology*, 02-06 June 1996, pp. 373-379. [Print]

[27] M. Munk, "Report No. 184 : The Aerodynamic Forces on Airship Hulls, " National Advisory Committee for Aeronautics, 1924. [Online] Available: http://naca.central.cranfield.ac.uk/reports/1924/naca-report-184.pdf. [Accessed: 14 November 2010].

[28] S. Hoerner and H. Borst, *Fluid Dynamic Lift*, Bakersfield, California, USA: Hoerner Fluid Dynamics, 1975. [Print]

[29] E. Lewis, Ed., *Principles of Naval Architecture Volume 2: Resistance, Propulsion and Vibration*, 2nd ed., Jersey City, New Jersey, USA: The Society of Naval Architects and Marine Engineers, 1988. [Print]

[30] T. Fossen and T. Perez, “Marine Systems Simulator (MSS),” developed at the Norwegian University of Science and Technology, 2010. [Online] Software Available: http://www.marinecontrol.org/. [Accessed: 5 March 2010].

[31] K. Ogata, *Modern Control Engineering*, 4th ed., Upper Saddle River, New Jersey, USA: Prentice Hall, 2002. [Print]

INITIAL DISTRIBUTION LIST

1. Defense Technical Information Center
   Ft. Belvoir, Virginia

2. Dudley Knox Library
   Naval Postgraduate School
   Monterey, California

3. Research Associate Professor Douglas P. Horner
   Center for Autonomous Vehicle Research (CAVR)
   Naval Postgraduate School
   Monterey, California

4. Professor Oleg Yakimenko
   Department of Mechanical and Aeronautical Engineering
   Naval Postgraduate School
   Monterey, California

5. Professor Isaac Kaminer
   Department of Mechanical and Aeronautical Engineering
   Naval Postgraduate School
   Monterey, California

6. Professor Thor I. Fossen
   Department of Engineering Cybernetics
   Norwegian University of Science and Technology, NTNU
   NO-7491 Trondheim, Norway